

# Monitoring Damage Accumulation in Continuous Fiber-Reinforced Ceramic-Matrix Composites with Different Fiber Preforms under Cyclic Loading Using Hysteresis-Based Damage Parameters

Li Longbiao\*

College of Civil Aviation, Nanjing University of Aeronautics and  
Astronautics, No.29 Yudao St., Nanjing 210016, PR China

received February 1, 2018; received in revised form February 12, 2018; accepted February 22, 2018

## Abstract

In this paper, the damage accumulation of continuous fiber-reinforced ceramic-matrix composites (CMCs) with different fiber preforms, i.e. 2D and 2.5D woven, 3D braided and needled C/SiC, 2D and 3D woven SiC/SiC composites, subject to cyclic tensile loading/unloading at room temperature has been investigated using the hysteresis-based damage parameters. Based on the damage mechanisms of matrix multiple cracking modes and relative frictional sliding between fibers and the matrix, the relationships between the hysteresis-based damage parameters and damage mechanisms of matrix cracking modes, fiber/matrix interface debonding/sliding have been established. The cyclic tensile loading/unloading stress/strain hysteresis loops, matrix cracking mode ratio and fiber/matrix interface sliding ratio of 2D and 2.5D woven, 3D braided and needled C/SiC, and 2D and 3D woven SiC/SiC composites have been predicted for different peak stresses. The comparisons of damage accumulation between C/SiC and SiC/SiC composites with different fiber preforms under cyclic tensile loading/unloading have been analyzed.

**Keywords:** Ceramic-matrix composites (CMCs), damage accumulation, matrix cracking, interface debonding, hysteresis loops.

## I. Introduction

Ceramic materials possess high specific strength and specific modulus at elevated temperatures. In spite of this, their use as structural components is severely limited owing to their brittleness. The continuous fiber-reinforced ceramic-matrix composites (CMCs) obtained by incorporating fibers in ceramic matrices, however, can be made as strong as metals, are lighter and can withstand much higher temperatures with increasing operating efficiency of aero engines, exceeding the capability of current nickel alloys typically used in high-pressure turbines<sup>1,2</sup>. CMC components, i.e. combustion chamber, turbine vanes/blades, and tail nozzles, have already been designed and tested in commercial aeroengines<sup>3,4</sup>. But these applications require very long lifetime in-service conditions. A big issue is therefore a better understanding of the damage mechanisms and kinetics in order to perform reliable life predictions.

Under cyclic loading, multiple damage mechanisms of transverse matrix cracking, fiber/matrix interface debonding/sliding and fibers break occur throughout the fiber-reinforced CMCs, leading to modulus and strength degradation<sup>5-19</sup>. The non-destructive testing (NDT) techniques used for damage monitoring of structural metallic components, i.e. optical microscopy, acoustic emission (AE), acousto-ultrasonic, ultrasonic C-scan, X-ray, thermography, eddy current and digital image correlation (DIC) have

been adapted to characterize CMCs at room or elevated temperature. Whitlow *et al.*<sup>20</sup> monitored the localized damage *in situ* and full-field surface strain of a 2D woven melt-infiltrated (MI) Hi-Nicalon<sup>TM</sup>SiC/SiC composite subjected to monotonic tensile loading using acoustic emission (AE) and digital image correlation (DIC) methods. The initiation and propagation of damage is related to strain field changes with increasing applied stress. Momon *et al.*<sup>21</sup> developed an acoustic emission-based technique to predict the residual fatigue life of two different types of CMCs, i.e. 2D woven chemical vapor infiltration (CVI) Hi-Nicalon<sup>TM</sup>-SiC/[Si-B-C] and ex PAN-HR<sup>TM</sup>/[Si-B-C] with PyC interface layer, at elevated temperatures in air condition. The elastic energy released under static fatigue tests was found to accelerate before ultimate failure, which allows prediction of the end of a static fatigue test from the AE activity. However, for the AE technique, it is necessary to monitor the material during all its service life, due to its sensitivity to transitions of state (i.e. a crack creation), and it cannot evaluate a damage state at zero stress without previous monitoring, which would be useful for maintenance. The electrical resistance (ER) provides a sensitive measure of internal damage in CMCs. Smith *et al.*<sup>22</sup> measured the electrical resistance of 2D woven Sylramic-iBN, Hi-Nicalon<sup>TM</sup> and Hi-Nicalon type S fibers-reinforced CVI SiC matrices with boron nitride (BN) interfaces subjected to cyclic tensile loading/unloading. The damage and maximum loading history can be recorded based on the residual resistance. Mansour *et*

\* Corresponding author: llb451@nuaa.edu.cn

*al.*<sup>23</sup> estimated the interlaminar crack length in 2D woven melt-infiltrated (MI) Hi-Nicalon<sup>TM</sup>-SiC/SiC composite at room temperature using electrical resistance. Simon *et al.*<sup>24</sup> investigated the damage evolution of 2D woven CVI Hi-Nicalon<sup>TM</sup>-SiC/[Si-B-C] composite subjected to cyclic tensile loading/unloading at room temperature with electrical resistance monitoring and acoustic emission recording. The evolution of the electrical resistivity during the interposed unload-reload cycles can give key information about the matrix crack density and the state of fiber/matrix interfaces. At an elevated temperature of 450 °C under oxidizing environments (i.e. ambient air and moist air with an imposed water pressure of 10 kPa), the electrical resistance is an accurate indicator of the damage of the PyC interphase in SiC/[Si-B-C] composite, which is sensitive to the oxidation environment<sup>25</sup>. Chateau *et al.*<sup>26</sup> characterized matrix cracking propagation and fiber breaking occurrence within a 1D CVI Hi-Nicalon type S SiC/SiC minicomposite using an *in situ* X-ray microtomography tensile test. Minor matrix cracks exist within the minicomposite and could become a transverse crack or remain localized. However, these minor matrix cracks have insignificant influence on the macro mechanical behavior compared to main matrix cracks. The application of these NDT methods mentioned above is based on the understanding of the macro mechanical behavior and microstructural damage inside of CMCs. The stress-strain hysteresis loops are another way to monitor the internal damage accumulation of CMCs. The damage mechanisms of matrix multicracking, fiber/matrix interface debonding/sliding and fiber fracture can be reflected on the hysteresis modulus, hysteresis width and hysteresis energy dissipation<sup>27-34</sup>. Campbell and Jenkins<sup>35</sup> used the hysteresis modulus degradation and hysteresis energy dissipation to investigate the thermal degradation of an oxide/oxide CMC. Mei<sup>36</sup> determined the thermal residual stress (TRS) of 2D woven CVI T300<sup>TM</sup>-C/SiC and Hi-Nicalon<sup>TM</sup>-SiC/SiC composites by solving the geometric intersection points of the regression lines of consecutive unloading/reloading hysteresis loops. Mei and Cheng<sup>11</sup> compared the mechanical hysteresis behavior of C/SiC composite with different fiber preforms. An effective coefficient of the fiber volume fraction in the direction of loading (ECFL) was used to characterize fiber architectures and preforms. Fantozzi and Reynaud<sup>37</sup> investigated the hysteresis behavior of bi- or multi-directional (cross-weave, cross-ply, 2.5D, [0/+60/-60]<sub>n</sub>) with SiC or C long fibers reinforced SiC, MAS-L, Si-B-C or C matrix at room and elevated temperatures in inert and oxidation conditions. However, the effect of matrix cracking modes on the hysteresis behavior of CMCs is not considered. Kuo and Chou<sup>38</sup> investigated the matrix multicracking in cross-ply CMCs, and divided the multiple matrix cracking states into five different modes, in which the matrix cracking mode 3 and mode 5 involve matrix cracking and fiber/matrix interface debonding/sliding in the longitudinal plies. Lamon<sup>39</sup> distinguished the matrix cracking in 2D woven CMCs into three main steps, and illustrated the schematic diagram showing the matrix cracking development. Under oxidizing environments, the matrix cracking

mode is critical with the formation of paths towards fibers and interphase for oxidizing volatile species (O<sub>2</sub>, H<sub>2</sub>O), contributing to a dramatic reduction in the mechanical properties<sup>40, 41, 42</sup>. However, in the researches mentioned above, the effect of multiple matrix cracking modes on the damage accumulation of CMCs with different fiber preforms is not considered.

The objective of this paper is to analyze the damage accumulation of C/SiC and SiC/SiC composites with different fiber preforms subjected to cyclic tensile loading/unloading at room temperature using the hysteresis-based damage parameters. Based on the damage mechanisms of matrix multiple cracking modes and relative frictional sliding between fibers and the matrix, the relationships between the hysteresis-based damage parameters (i.e. the hysteresis dissipated energy, hysteresis modulus and fiber/matrix interface sliding ratio) and damage mechanisms of matrix multicracking modes, fiber/matrix interface debonding/sliding are established. The cyclic loading/unloading tensile stress/strain hysteresis loops, matrix cracking mode ratio and fiber/matrix interface sliding ratio of 2D and 2.5D woven, 3D braided and needled C/SiC, and 2D and 3D SiC/SiC composites are predicted for different peak stresses. The comparisons of damage accumulation of C/SiC and SiC/SiC composites with different fiber preforms under cyclic tensile loading/unloading are analyzed.

## II. Theoretical Analysis

If matrix cracking and fiber/matrix interface debonding are present upon first loading, the stress/strain hysteresis loops develop as a result of energy dissipation through frictional sliding between fibers and the matrix upon unloading/reloading<sup>43-47</sup>. The shape, location and area of the stress/strain hysteresis loops depend upon the fiber/matrix interface debonding and frictional sliding. Under cyclic loading, matrix cracking in 2D or 3D CMCs can be divided into five different modes, as shown in Fig. 1, including:

- (1) Matrix cracking mode 1: transverse cracking in the transverse yarns;
- (2) Matrix cracking mode 2: transverse cracking and matrix cracking occurring in the transverse and longitudinal yarns with perfect interface bonding in the longitudinal yarns;
- (3) Matrix cracking mode 3: transverse cracking and matrix cracking occurring in the transverse and longitudinal yarns with interface debonding in the longitudinal yarns;
- (4) Matrix cracking mode 4: matrix cracking in the longitudinal yarns with interface bonding;
- (5) Matrix cracking mode 5: matrix cracking in the longitudinal yarns with interface debonding.

The difference between the matrix cracking mode 2 and mode 4, or mode 3 and mode 5, is that only the matrix cracking in the longitudinal yarns occurs, and the transverse cracking does not appear in the transverse yarns at the location where matrix cracking appears corresponding to mode 4 or mode 5; and the difference between mode 2 and mode 3, or mode 4 and mode 5, is that the fiber/matrix interface debonding occurs in the longitudinal yarns corresponding to the cracking mode 3 and mode 5.

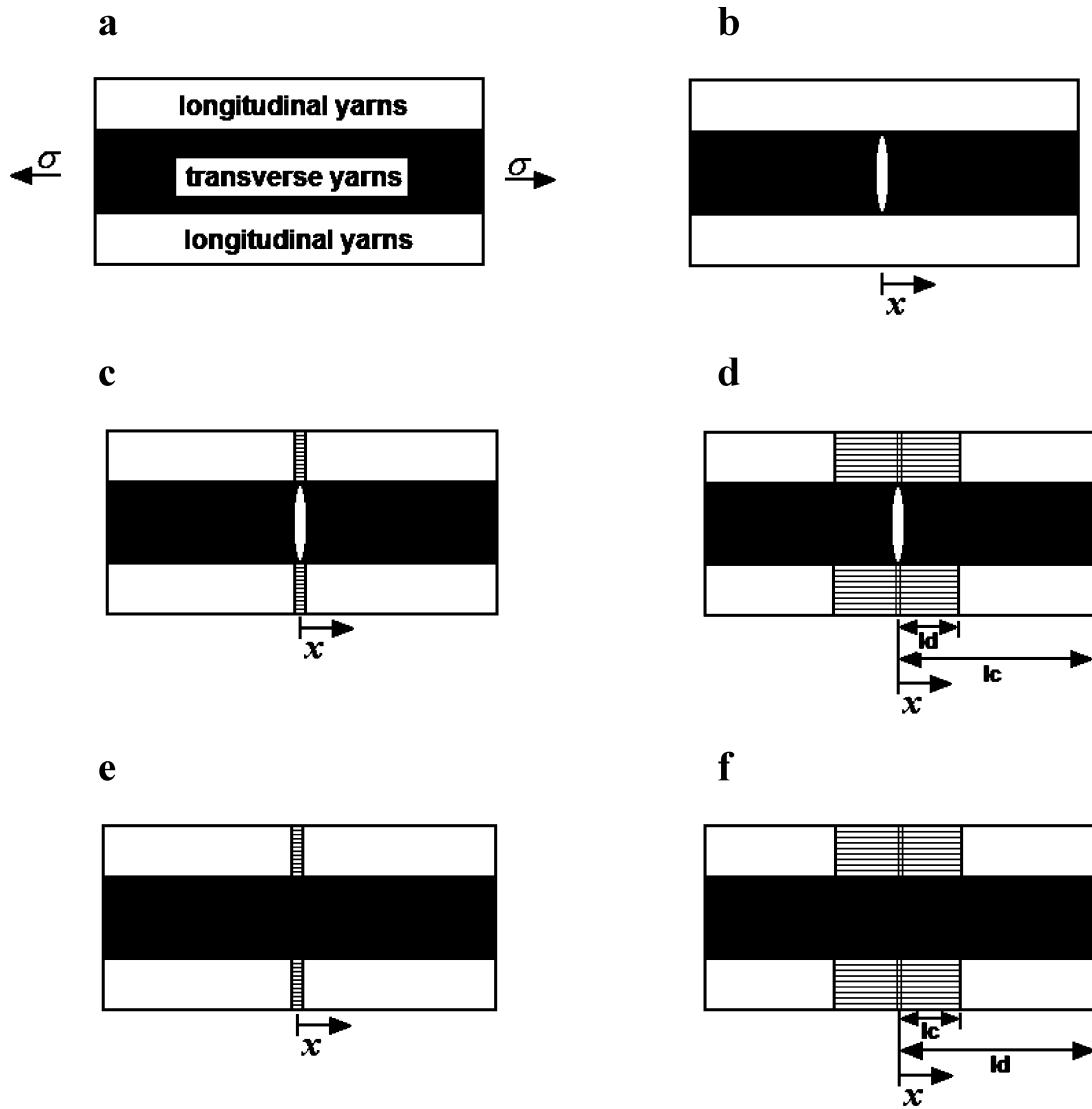


**Fig. 1:** The undamaged state and five damaged modes of CMCs (a) undamaged composite; (b) mode 1: transverse cracking; (c) mode 2: transverse cracking and matrix cracking with perfect fiber/matrix bonding; (d) mode 3: transverse cracking and matrix cracking with fiber/matrix interface debonding; (e) mode 4: matrix cracking with perfect fiber/matrix bonding; and (f) mode 5: matrix cracking with fiber/matrix debonding.

Based on the damage mechanisms of matrix multicracking, fiber/matrix interface debonding/sliding upon unloading/reloading, the stress/strain hysteresis loops in 2D or 3D CMCs for matrix cracking mode 3 and mode 5 can be divided into four different cases, as following:

- (1) Case 1: the fiber/matrix interface partially debonding and the fiber sliding completely relative to the matrix in the fiber/matrix interface debonded region;
- (2) Case 2: the fiber/matrix interface partially debonding and the fiber sliding partially relative to the matrix in the fiber/matrix interface debonded region;
- (3) Case 3: the fiber/matrix interface completely debonding and the fiber sliding partially relative to thematrix in the fiber/matrix interface debonded region;
- (4) Case 4: the fiber/matrix interface completely debonding and the fiber sliding completely relative to the matrix in the fiber/matrix interface debonded region.

#### (1) Hysteresis models for matrix cracking mode 3

When the fiber/matrix interface partially debonds, the unit cell of the longitudinal yarn can be divided into two

regions, i.e. fiber/matrix interface debonded region and interface bonded region. Upon unloading, counter slip occurs at the matrix crack plane over a distance  $y$ , which is defined as the fiber/matrix interface counter-slip length. The fiber/matrix interface debonded region can be divided into two regions, i.e. fiber/matrix interface counter-slip region and interface slip region. Upon reloading, new slip occurs near matrix crack plane over a distance  $z$ , which is denoted to be the fiber/matrix interface new-slip region. The fiber axial stress distributions for matrix cracking mode 3 corresponding to the fiber/matrix interface slip Cases 1 - 4 are given in Fig. 2.

When the fiber/matrix interface partially debonds, the unloading strain ( $\epsilon_{cu}$ ) and reloading strain ( $\epsilon_{cr}$ ) corresponding to the fiber/matrix interface slip Case 1 and Case 2 are determined using the following equations.

$$\epsilon_{cu} = \frac{\sigma}{V_{f\_axial} E_f} + 4 \frac{\tau_i}{E_f} \frac{y^2}{r_f l_c} - 2 \frac{\tau_i}{E_f} \frac{(2y - l_d)(2y - l_c + l_d)}{r_{fc}} - (\alpha_c - \alpha_f) \Delta T \quad (1)$$

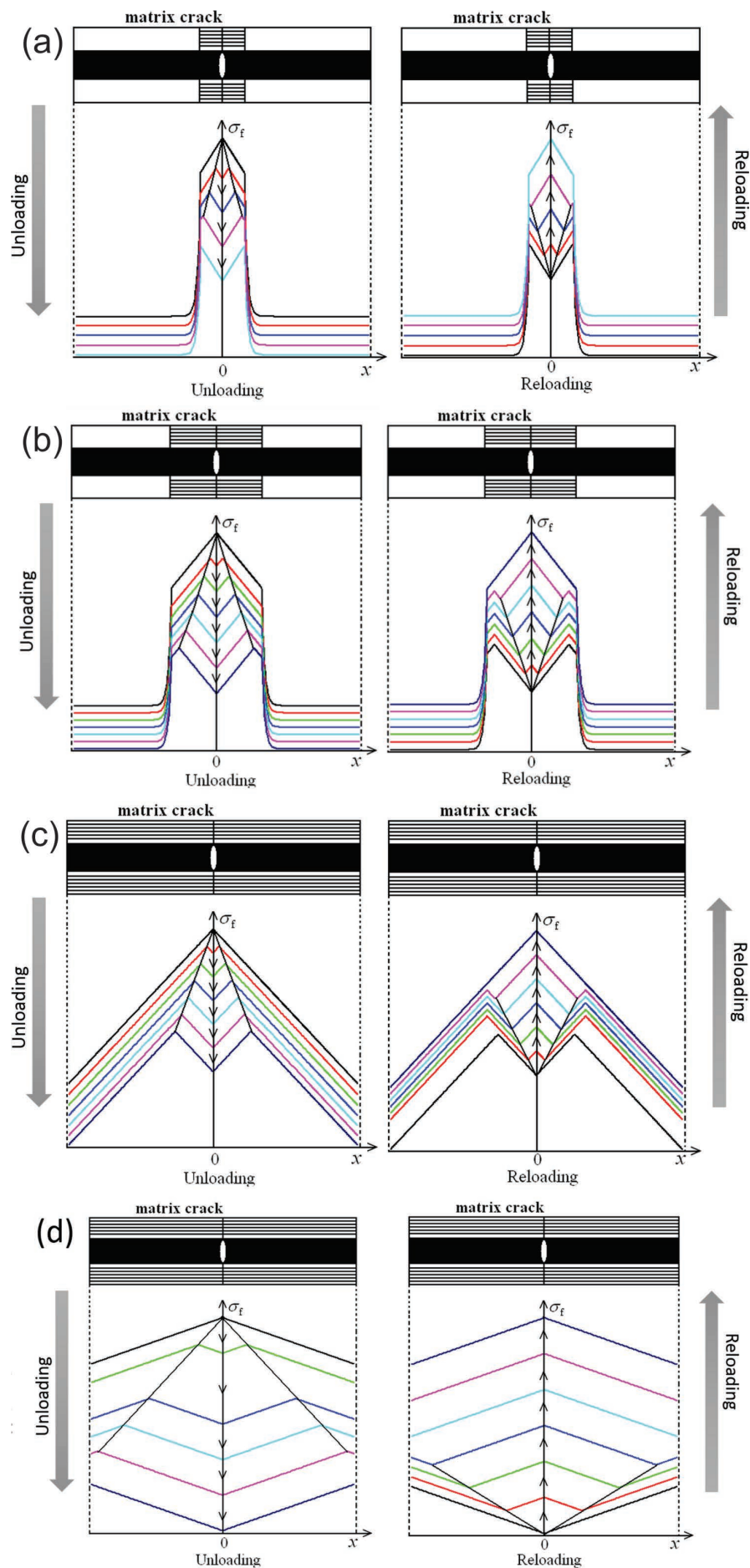


**Fig. 2:** The fiber axial stress distribution for matrix cracking mode 3 upon unloading and reloading corresponding to fiber/matrix interface slip cases of (a) Case 1; (b) Case 2; (c) Case 3; and (d) Case 4.

$$\epsilon_{cr} = \frac{\sigma}{V_{f\_axial} E_f} - 4 \frac{\tau_i}{E_f} \frac{z^2}{r_f l_c} + \frac{4\tau_i}{E_f} \frac{(y-2z)^2}{r_f l_c} + 2 \frac{\tau_i}{E_f} \frac{(l_d - 2y + 2z)(l_d + 2y - 2y - l_c)}{r_f l_c} - (\alpha_c - \alpha_f) \Delta T \quad (2)$$

where  $V_{f\_axial}$  denotes the fiber volume content along the longitudinal direction;  $E_f$  denotes the fiber elastic modulus;  $r_f$  denotes the fiber radius;  $\tau_i$  denotes the fiber/matrix interface shear stress in the longitudinal yarns;  $l_c$  denotes the matrix crack spacing;  $l_d$  denotes the fiber/matrix interface debonded length;  $a_f$  and  $a_c$  denote the fiber and composite thermal expansion coefficient, respectively; and  $\Delta T$  denotes the temperature difference between the fabricated temperature  $T_0$  and testing temperature  $T_1$  ( $\Delta T = T_1 - T_0$ ).

When the fiber/matrix interface completely debonds, the unloading strain ( $\epsilon_{cu}$ ) and reloading strain ( $\epsilon_{cr}$ ) corresponding to the fiber/matrix interface slip Case 3 and Case 4 are determined using the following equations.

$$\epsilon_{cu} = \frac{\sigma}{V_{f\_axial} E_f} + 4 \frac{\tau_i}{E_f} \frac{y^2}{r_f l_c} - 2 \frac{\tau_i}{E_f} \frac{(2y - l_c/2)^2}{r_f l_c} - (\alpha_c - \alpha_f) \Delta T \quad (3)$$

$$\epsilon_{cr} = \frac{\sigma}{V_{f\_axial} E_f} - 4 \frac{\tau_i}{E_f} \frac{z^2}{r_f l_c} + \frac{4\tau_i}{E_f} \frac{(y-2z)^2}{r_f l_c} - 2 \frac{\tau_i}{E_f} \frac{(l_c/2 - 2y + 2z)^2}{r_f l_c} - (\alpha_c - \alpha_f) \Delta T \quad (4)$$

## (2) Hysteresis models of matrix cracking mode 5

For matrix cracking mode 5, the fiber axial stress distributions corresponding to the fiber/matrix interface slip Cases 1 - 4 are shown in Fig. 3. The unloading strain ( $\epsilon_{cu}$ ) and reloading strain ( $\epsilon_{cr}$ ) corresponding to the fiber/matrix interface slip Case 1 and Case 2 are determined using the following equations.

$$\epsilon_{cu} = \frac{1}{V_{f\_axial} E_f} (\sigma - k\sigma_{to}) + 4 \frac{\tau_i}{E_f} \frac{y^2}{r_f l_c} - 2 \frac{\tau_i}{E_f} \frac{(2y - l_d)(2y + l_d - l_c)}{r_f l_c} - (\alpha_c - \alpha_f) \Delta T \quad (5)$$

$$\epsilon_{cr} = \frac{1}{V_{f\_axial} E_f} (\sigma - k\sigma_{to}) - 4 \frac{\tau_i}{E_f} \frac{z^2}{r_f l_c} + \frac{4\tau_i}{E_f} \frac{(y-2z)^2}{r_f l_c} + 2 \frac{\tau_i}{E_f} \frac{(l_d - 2y + 2z)(l_d + 2y - 2z - l_c)}{r_f l_c} - (\alpha_c - \alpha_f) \Delta T \quad (6)$$

where  $k$  denotes the proportion of transverse yarns in the entire composite.

When the fiber/matrix interface completely debonds, the unloading strain ( $\epsilon_{cu}$ ) and reloading strain ( $\epsilon_{cr}$ ) corresponding to the fiber/matrix interface slip Case 3 and Case 4 are determined using the following equations.

$$\epsilon_{cu} = \frac{1}{V_{f\_axial} E_f} (\sigma - k\sigma_{to}) + 4 \frac{\tau_i}{E_f} \frac{y^2}{r_f l_c} - 2 \frac{\tau_i}{E_f} \frac{(2y - l_c/2)^2}{r_f l_c} - (\alpha_c - \alpha_f) \Delta T \quad (7)$$

$$\epsilon_{cr} = \frac{1}{V_{f\_axial} E_f} (\sigma - k\sigma_{to}) - 4 \frac{\tau_i}{E_f} \frac{z^2}{r_f l_c} + \frac{4\tau_i}{E_f} \frac{(y-2z)^2}{r_f l_c} - 2 \frac{\tau_i}{E_f} \frac{(l_c/2 - 2y + 2z)^2}{r_f l_c} - (\alpha_c - \alpha_f) \Delta T \quad (8)$$

## (3) Hysteresis-based damage parameters

Considering the effect of multiple matrix cracking modes, the composite unloading and reloading strains are described using the following equations.

$$(\epsilon_u)_c = \eta(\epsilon_{cu})_3 + (1 - \eta)(\epsilon_{cu})_5 \quad (9)$$

$$(\epsilon_r)_c = \eta(\epsilon_{cr})_3 + (1 - \eta)(\epsilon_{cr})_5 \quad (10)$$

where  $(\epsilon_u)_c$  and  $(\epsilon_r)_c$  denote the unloading and reloading strain of the composite, respectively;  $(\epsilon_{cu})_3$  and  $(\epsilon_{cr})_3$  denote the unloading and reloading strain of matrix cracking mode 3, respectively;  $(\epsilon_{cu})_5$  and  $(\epsilon_{cr})_5$  denote the unloading and reloading strain of matrix cracking mode 5, respectively; and  $\eta$  is the damage parameter determined based on the composite damage condition, i.e. the proportion of cracking mode 3 in the entire of matrix cracking modes of the composite,  $\eta \in [0, 1]$ .

Upon cyclic loading, the area associated with the stress/strain hysteresis loops is the energy lost during the corresponding cycle, which is defined using the following equation.

$$U = \int_{\sigma_{min}}^{\sigma_{max}} [\epsilon_u(\sigma) - \epsilon_r(\sigma)] d\sigma \quad (11)$$

The hysteresis dissipated energy of matrix cracking mode 3 and mode 5 can be derived by inserting corresponding unloading and reloading strains into Eq. (11). The composite hysteresis dissipated energy is determined using the following equation.

$$U_c = \eta U_3 + (1 - \eta) U_5 \quad (12)$$

where  $U_3$  and  $U_5$  denote the hysteresis dissipated energy of matrix cracking mode 3 and mode 5, respectively.

Under cyclic loading, the hysteresis modulus is determined using the following equation.

$$E_a = \frac{\sigma_{max} - \sigma_{min}}{\epsilon_{max} - \epsilon_{min}} \quad (13)$$

where  $\sigma_{max}$  and  $\sigma_{min}$  denote the peak and valley stresses, respectively; and  $\epsilon_{max}$  and  $\epsilon_{min}$  denote the fatigue peak and valley strains, respectively.

## III. Experimental Comparisons

The damage accumulation of 2D and 2.5D woven, 3D braided and needled C/SiC, 2D woven SiC/SiC and SiC/[Si-B-C], and 3D woven SiC/SiC composites subjected to cyclic tensile loading/unloading are analyzed using the hysteresis-based damage parameters, i.e. the hysteresis dissipated energy, hysteresis modulus and fiber/matrix interface sliding ratio.

### (1) 2D and 2.5D woven, 3D braided and needled C/SiC composites

Wang *et al.*<sup>7</sup> investigated the cyclic tensile loading/unloading behavior of 2D woven CVI T300<sup>TM</sup>-C/SiC composite at room temperature. The monotonic tensile stress/strain curve of 2D woven C/SiC is shown in Fig. 4, and the composite tensile strength is about 245 MPa and the failure strain is 0.69 %. The composite is cyclic loading/unloading at different peak stresses of 90, 110, 130, 150, 170, 190 and 210 MPa, as shown in Fig. 5. With increasing peak stress, the damage parameter  $\eta$  (i.e., the proportion of matrix cracking mode 3) increases from  $\eta = 0.3$  at the peak stress of  $\sigma_{max} = 90$  MPa to  $\eta = 0.7$  at the peak stress



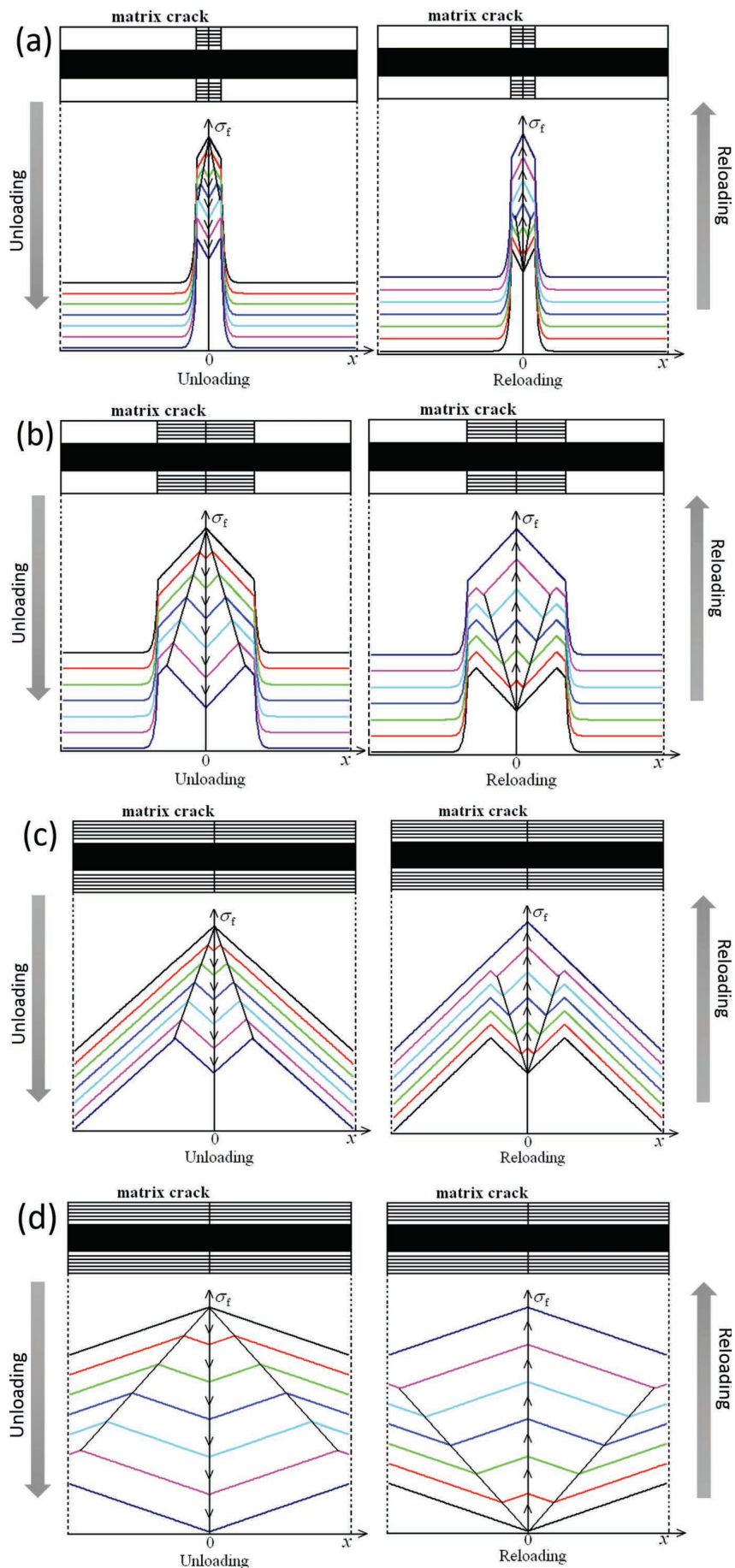


**Fig. 3:** The fiber axial stress distribution for matrix cracking mode 5 upon unloading and reloading corresponding to fiber/matrix interface slip cases of (a) Case 1; (b) Case 2; (c) Case 3; and (d) Case 4.

of  $\sigma_{\max} = 210$  MPa, as shown in Fig. 5a-g; the hysteresis dissipated energy increases from  $U_c = 4.4$  kPa at the peak stress of  $\sigma_{\max} = 90$  MPa to  $U_c = 39.7$  kPa at the peak stress of  $\sigma_{\max} = 210$  MPa; the hysteresis modulus decreases from  $E_a = 81.7$  GPa at the peak stress of  $\sigma_{\max} = 90$  MPa to  $E_a = 55.9$  GPa at the peak stress of  $\sigma_{\max} = 210$  MPa; the fiber/matrix interface debonding ratio ( $y/l_d$  and  $z/l_d$ ) corresponds to the fiber/matrix interface slip Case 2 at the peak stresses of  $\sigma_{\max} = 90, 110$  and  $130$  MPa, and the fiber/matrix interface slip Case 4 at the peak stresses of  $\sigma_{\max} = 150, 170, 190$  and  $210$  MPa for matrix cracking mode 3, as shown in Fig. 6a-g; and for matrix cracking mode 5, the fiber/matrix interface debonding ratio ( $y/l_d$  and  $z/l_d$ ) corresponds to the fiber/matrix interface slip Case 1 at the peak stresses of  $\sigma_{\max} = 90, 110, 130$  and  $150$  MPa, and the fiber/matrix interface slip Case 2 at the peak stresses of  $\sigma_{\max} = 170, 190$  and  $210$  MPa, as shown in Fig. 6a-g.

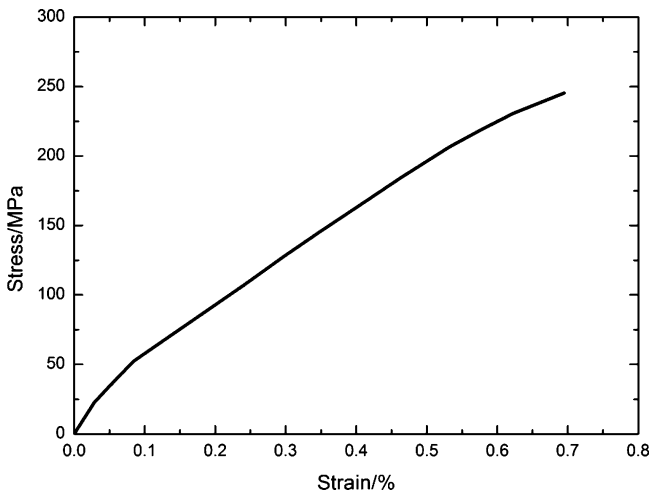


Fig. 4: The monotonic tensile stress/strain curve of 2D woven C/SiC composite<sup>7</sup>.

Chang *et al.*<sup>10</sup> investigated the cyclic tensile loading/unloading behavior of 2.5D woven CVI T300<sup>TM</sup>-C/SiC composite at room temperature. The monotonic tensile stress/strain curves of 2.5D woven C/SiC composite along the warp and weft direction are given in Fig. 7. Along the warp direction, the composite tensile strength is about 334 MPa and the failure strain is 0.72 %; and along the weft direction, the composite tensile strength is about 136 MPa and the failure strain is 0.7 %. Under cyclic tensile loading/unloading along the warp direction, the stress/strain hysteresis loops of 2.5D woven C/SiC at different peak stresses of  $\sigma_{\max} = 110, 127, 142, 160, 180$  and  $325$  MPa are shown in Fig. 8a-f; with increasing peak stress, the damage parameter  $\eta$  (i.e., the proportion of matrix cracking mode 3) increases from  $\eta = 0.2$  at the peak stress of  $\sigma_{\max} = 110$  MPa to  $\eta = 0.55$  at the peak stress of  $\sigma_{\max} = 325$  MPa; the hysteresis dissipated energy increases from  $U_c = 2.8$  kPa at the peak stress of  $\sigma_{\max} = 110$  MPa to  $U_c = 89.8$  kPa at the peak stress of  $\sigma_{\max} = 325$  MPa; the hysteresis modulus decreases from  $E_a = 135$  GPa at the peak stress of  $\sigma_{\max} = 110$  MPa to  $E_a = 74.9$  GPa at the peak stress of  $\sigma_{\max} = 325$  MPa; the fiber/matrix interface debonding ratio ( $y/l_d$  and  $z/l_d$ ) corresponds to the fiber/matrix interface slip Case 1 at the peak stress of  $\sigma_{\max} = 110$  MPa, and the fiber/matrix interface slip

Case 2 at the peak stresses of  $\sigma_{\max} = 127, 142, 160, 180$  and  $325$  MPa for matrix cracking mode 3, as shown in Fig. 9a-f; and for matrix cracking mode 5, the fiber/matrix interface debonding ratio ( $y/l_d$  and  $z/l_d$ ) corresponds to the fiber/matrix interface slip Case 1 at the peak stresses of  $\sigma_{\max} = 110, 127, 142, 160$  and  $180$  MPa, and the fiber/matrix interface slip Case 2 at the peak stress of  $\sigma_{\max} = 325$  MPa, as shown in Fig. 9a-f. Under cyclic tensile loading/unloading along the weft direction, the stress/strain hysteresis loops of 2.5D C/SiC at different peak stresses of  $\sigma_{\max} = 56, 77, 96$  and  $134$  MPa are shown in Fig. 10a-d; with increasing peak stress, the damage parameter  $\eta$  (i.e., the proportion of matrix cracking mode 3) increases from  $\eta = 0.2$  at the peak stress of  $\sigma_{\max} = 56$  MPa to  $\eta = 0.4$  at the peak stress of  $\sigma_{\max} = 134$  MPa; the hysteresis dissipated energy increases from  $U_c = 1.8$  kPa at the peak stress of  $\sigma_{\max} = 56$  MPa to  $U_c = 31.4$  kPa at the peak stress of  $\sigma_{\max} = 134$  MPa; the hysteresis modulus decreases from  $E_a = 51.2$  GPa at the peak stress of  $\sigma_{\max} = 56$  MPa to  $E_a = 31.6$  GPa at the peak stress of  $\sigma_{\max} = 134$  MPa; the fiber/matrix interface debonding ratio ( $y/l_d$  and  $z/l_d$ ) corresponds to the fiber/matrix interface slip Case 1 at the peak stresses of  $\sigma_{\max} = 56$  and  $77$  MPa, and the fiber/matrix interface slip Case 2 at the peak stresses of  $\sigma_{\max} = 96$  and  $134$  MPa for matrix cracking mode 3, as shown in Fig. 11a-d; and for matrix cracking mode 5, the fiber/matrix interface debonding ratio ( $y/l_d$  and  $z/l_d$ ) corresponds to the fiber/matrix interface slip Case 1 at the peak stresses of  $\sigma_{\max} = 56$  and  $77$  MPa, and the fiber/matrix interface slip Case 2 at the peak stress of  $\sigma_{\max} = 96$  and  $134$  MPa, as shown in Fig. 11a-d.

Mei and Cheng<sup>11</sup> investigated the cyclic tensile loading/unloading behavior of 3D braided CVI T300<sup>TM</sup>-C/SiC composite at room temperature. The monotonic tensile stress/strain curve of 3D braided C/SiC composite is given in Fig. 12. The composite tensile strength is about 308 MPa and the failure strain is 0.6 %. Under cyclic tensile loading/unloading, the stress/strain hysteresis loops of 3D braided C/SiC at different peak stresses of  $\sigma_{\max} = 245, 260, 275$  and  $300$  MPa are shown in Fig. 13a-d; with increasing peak stress, the damage parameter  $\eta$  (i.e., the proportion of matrix cracking mode 3) increases from  $\eta = 0.4$  at the peak stress of  $\sigma_{\max} = 245$  MPa to  $\eta = 0.55$  at the peak stress of  $\sigma_{\max} = 300$  MPa; the hysteresis dissipated energy increases from  $U_c = 35.1$  kPa at the peak stress of  $\sigma_{\max} = 245$  MPa to  $U_c = 76.2$  kPa at the peak stress of  $\sigma_{\max} = 300$  MPa; the hysteresis modulus decreases from  $E_a = 70.5$  GPa at the peak stress of  $\sigma_{\max} = 245$  MPa to  $E_a = 59.1$  GPa at the peak stress of  $\sigma_{\max} = 300$  MPa; the fiber/matrix interface debonding ratio ( $y/l_d$  and  $z/l_d$ ) corresponds to the fiber/matrix interface slip Case 1 at the peak stresses of  $\sigma_{\max} = 245, 260$  and  $270$  MPa, and the fiber/matrix interface slip Case 2 at the peak stresses of  $\sigma_{\max} = 300$  MPa for matrix cracking mode 3, as shown in Fig. 14a-d; and for matrix cracking mode 5, the fiber/matrix interface debonding ratio ( $y/l_d$  and  $z/l_d$ ) corresponds to the fiber/matrix interface slip Case 1 at the peak stresses of  $\sigma_{\max} = 245, 260$  and  $270$  MPa, and the fiber/matrix interface slip Case 2 at the peak stress of  $\sigma_{\max} = 300$  MPa, as shown in Fig. 14a-d.

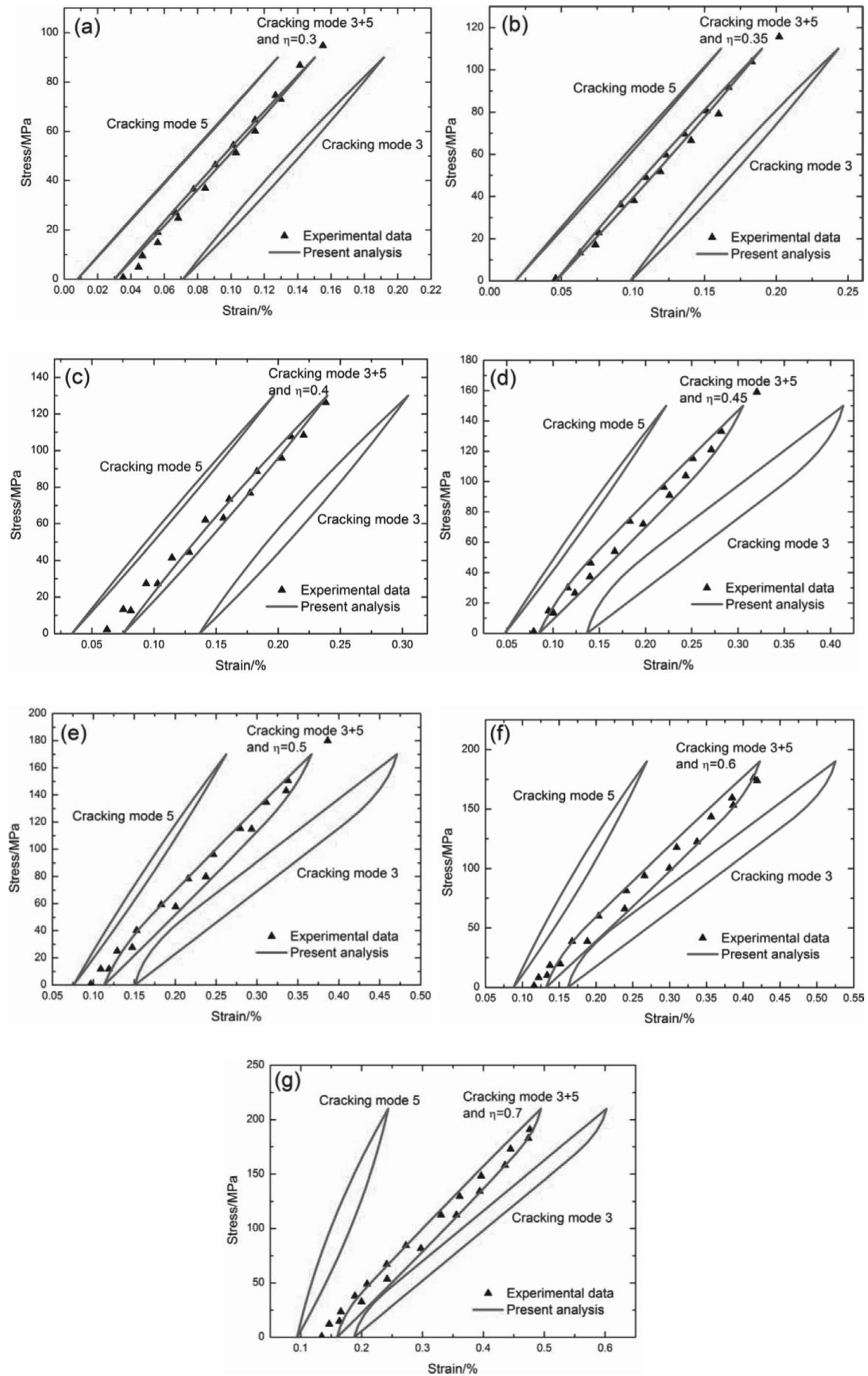
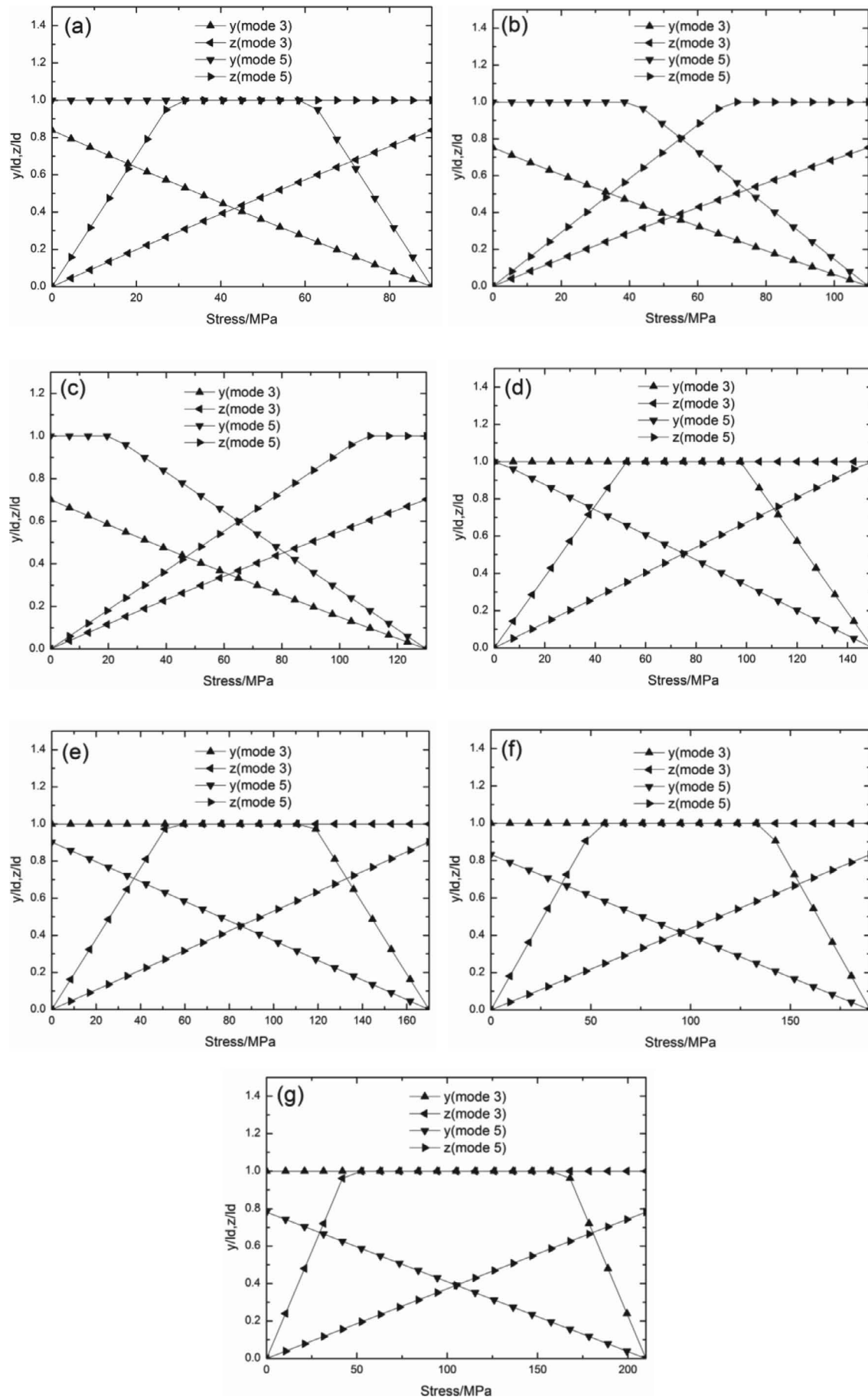


Fig. 5: The theoretical and experimental stress/strain hysteresis loops of 2D woven C/SiC composite 7 corresponding to different peak stresses of (a)  $\sigma_{\max} = 90$  MPa; (b)  $\sigma_{\max} = 110$  MPa; (c)  $\sigma_{\max} = 130$  MPa; (d)  $\sigma_{\max} = 150$  MPa; (e)  $\sigma_{\max} = 170$  MPa; (f)  $\sigma_{\max} = 190$  MPa; and (g)  $\sigma_{\max} = 210$  MPa.





**Fig. 6:** The fiber/matrix interface sliding ratio ( $y/l_d$  and  $z/l_d$ ) of 2D woven C/SiC composite corresponding to different peak stresses of (a)  $\sigma_{\max} = 90$  MPa; (b)  $\sigma_{\max} = 110$  MPa; (c)  $\sigma_{\max} = 130$  MPa; (d)  $\sigma_{\max} = 150$  MPa; (e)  $\sigma_{\max} = 170$  MPa; (f)  $\sigma_{\max} = 190$  MPa; and (g)  $\sigma_{\max} = 210$  MPa.

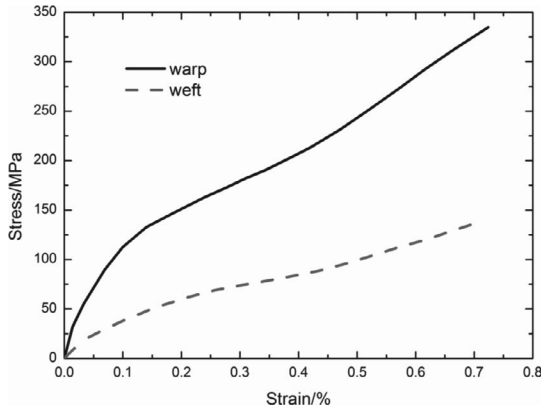


Fig. 7: The monotonic tensile stress/strain curve of 2.5D woven C/SiC composite along the warp and weft direction<sup>10</sup>.

## (2) 3D needled C/SiC composite

Xie *et al.*<sup>13</sup> investigated the cyclic tensile loading/unloading behavior of 3D needled chemical vapor infiltration (CVI)/polymer impregnation-pyrolysis (PIP)/liquid silicon infiltration processes (LSI) T300™-C/SiC composite at room temperature. The monotonic tensile stress/strain curve is shown in Fig. 15. The composite tensile strength is about 104 MPa and the failure strain is 0.45 %. Under cyclic tensile loading/unloading, the stress/strain hysteresis loops of 3D needled C/SiC at different peak stresses of  $\sigma_{\max} = 45, 55, 65$  and 90 MPa are shown in Fig. 16a-d;

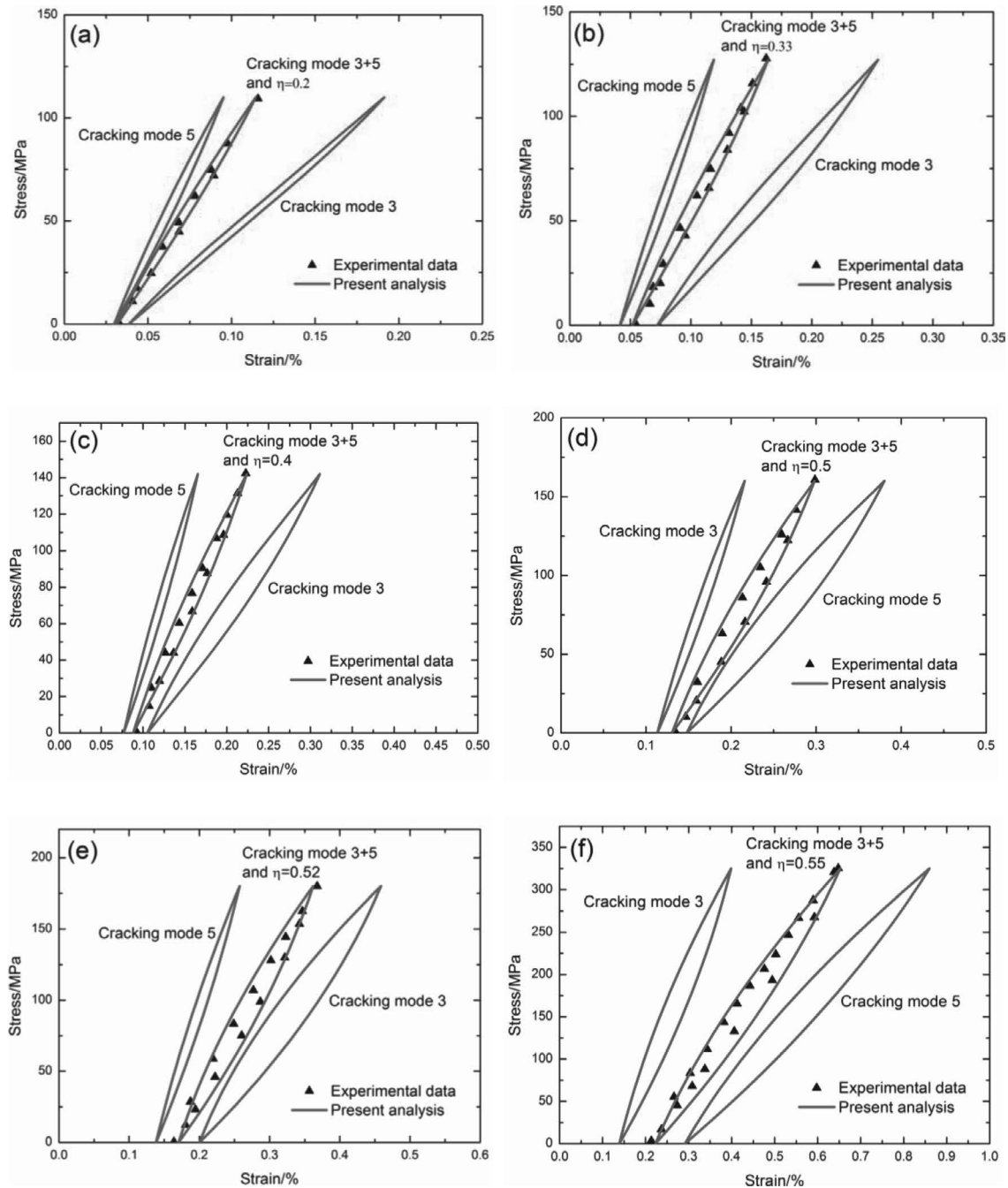
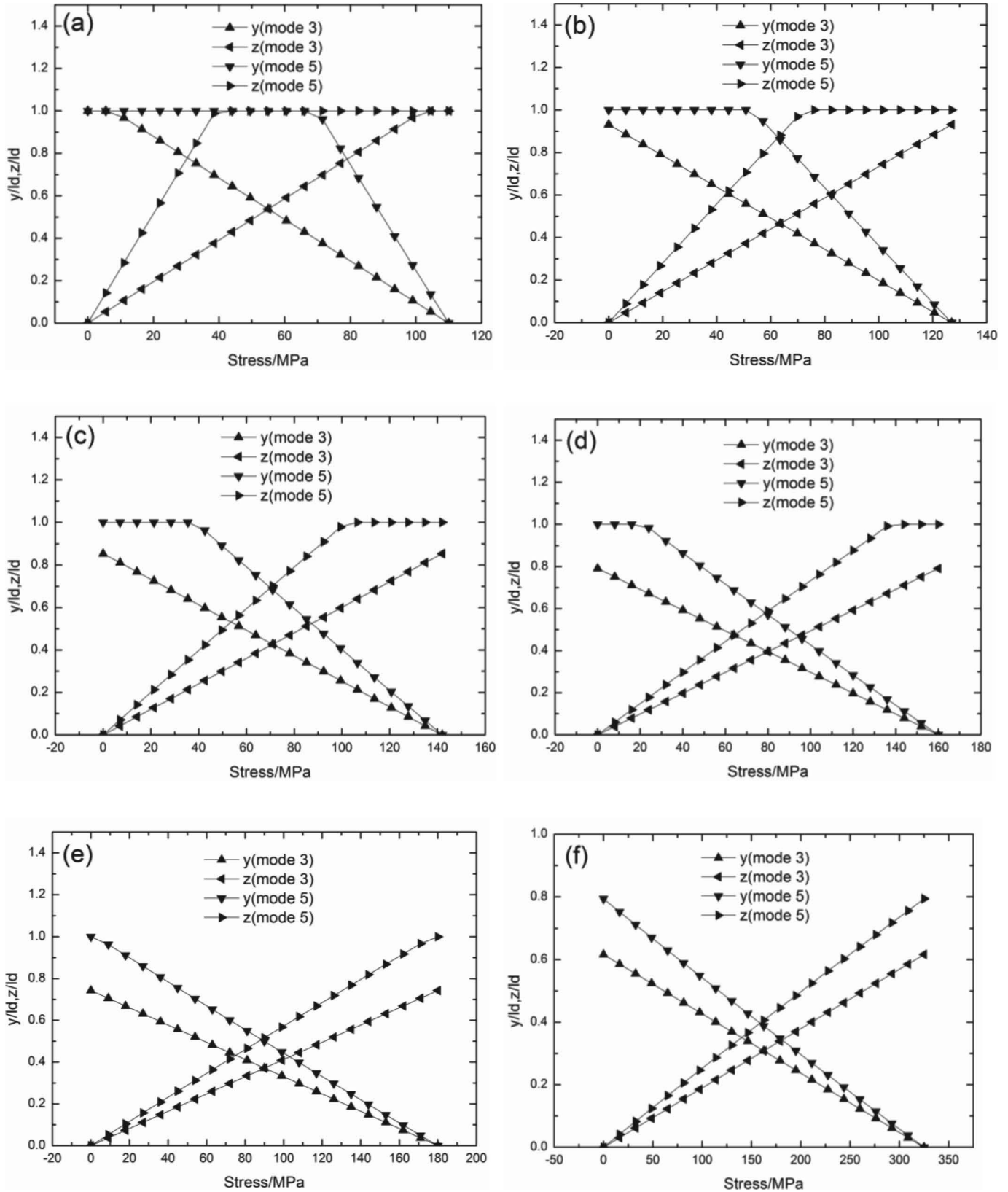


Fig. 8: The theoretical and experimental stress/strain hysteresis loops of 2.5D woven C/SiC composite<sup>10</sup> under cyclic loading along the warp direction corresponding to different peak stresses of (a)  $\sigma_{\max} = 110$  MPa; (b)  $\sigma_{\max} = 127$  MPa; (c)  $\sigma_{\max} = 142$  MPa; (d)  $\sigma_{\max} = 160$  MPa; (e)  $\sigma_{\max} = 180$  MPa; and (f)  $\sigma_{\max} = 325$  MPa.



**Fig. 9:** The fiber/matrix interface sliding ratio ( $y/l_d$  and  $z/l_d$ ) of 2.5D woven C/SiC composite under cyclic loading along the warp direction corresponding to different peak stresses of (a)  $\sigma_{\max} = 110$  MPa; (b)  $\sigma_{\max} = 127$  MPa; (c)  $\sigma_{\max} = 142$  MPa; (d)  $\sigma_{\max} = 160$  MPa; (e)  $\sigma_{\max} = 180$  MPa; and (f)  $\sigma_{\max} = 325$  MPa.

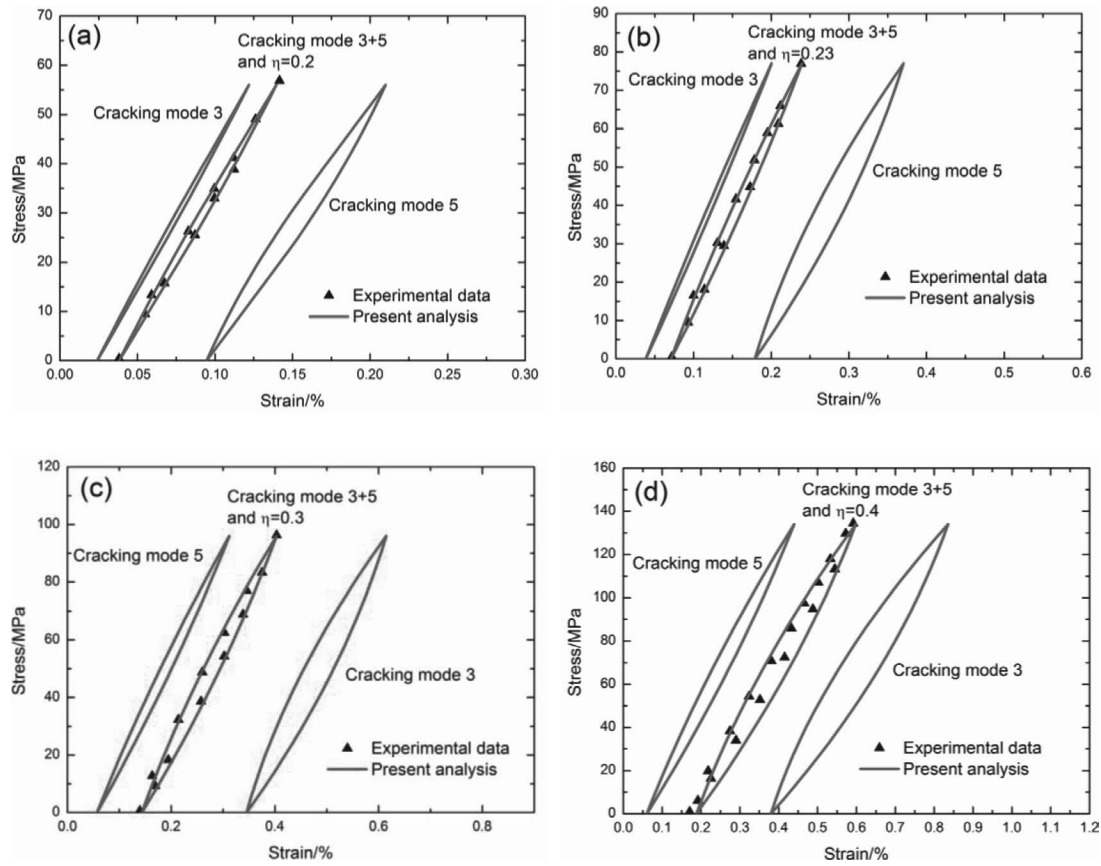


Fig. 10: The theoretical and experimental stress/strain hysteresis loops of 2.5D woven C/SiC composite<sup>10</sup> under cyclic loading along the weft direction corresponding to different peak stresses of (a)  $\sigma_{\max} = 56$  MPa; (b)  $\sigma_{\max} = 77$  MPa; (c)  $\sigma_{\max} = 96$  MPa; and (d)  $\sigma_{\max} = 134$  MPa.

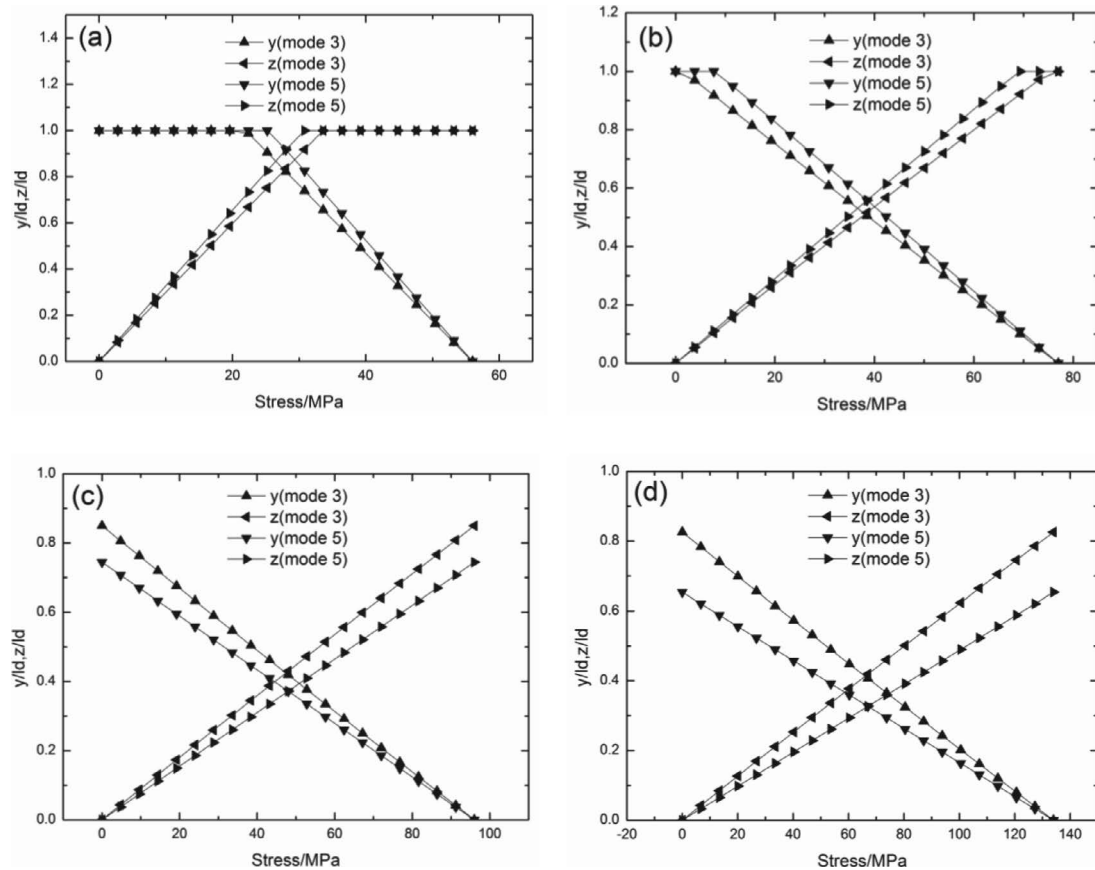


Fig. 11: The fiber/matrix interface sliding ratio ( $y/l_d$  and  $z/l_d$ ) of 2.5D woven C/SiC composite under cyclic loading along the weft direction corresponding to different peak stresses of (a)  $\sigma_{\max} = 56$  MPa; (b)  $\sigma_{\max} = 77$  MPa; (c)  $\sigma_{\max} = 96$  MPa; and (d)  $\sigma_{\max} = 134$  MPa.

with increasing peak stress, the damage parameter  $\eta$  (i.e. the proportion of matrix cracking mode 3) increases from  $\eta = 0.1$  at the peak stress of  $\sigma_{\max} = 45$  MPa to  $\eta = 0.25$  at the peak stress of  $\sigma_{\max} = 90$  MPa; the hysteresis dissipated energy increases from  $U_c = 1.8$  kPa at the peak stress of  $\sigma_{\max} = 45$  MPa to  $U_c = 10.8$  kPa at the peak stress of  $\sigma_{\max} = 90$  MPa; the hysteresis modulus decreases from  $E_a = 33.7$  GPa at the peak stress of  $\sigma_{\max} = 45$  MPa to  $E_a = 25.7$  GPa at the peak stress of  $\sigma_{\max} = 90$  MPa; the fiber/matrix interface debonding ratio ( $y/l_d$  and  $z/l_d$ ) corresponds to the fiber/matrix interface slip Case 1 at the peak stress of  $\sigma_{\max} = 45$  MPa, and the fiber/matrix interface slip Case 2 at the peak stresses of  $\sigma_{\max} = 55, 65$  and  $90$  MPa for matrix cracking mode 3, as shown in Fig. 17a-d; and for matrix cracking mode 5, the fiber/matrix interface debonding ratio ( $y/l_d$  and  $z/l_d$ ) corresponds to the fiber/matrix interface slip Case 1 at the peak stresses of  $\sigma_{\max} = 45$  and  $55$  MPa, and the fiber/matrix interface slip Case 2 at the peak stresses of  $\sigma_{\max} = 65$  and  $90$  MPa, as shown in Fig. 17a-d.

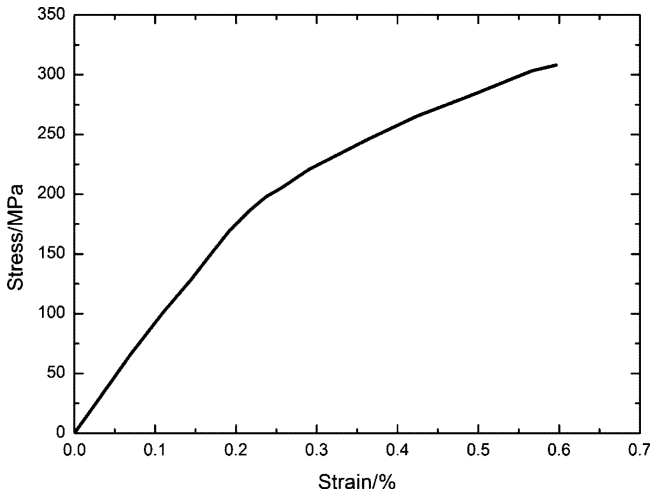


Fig. 12: The monotonic tensile stress/strain curve of 3D braided C/SiC composite <sup>11</sup>.

### (3) 2D and 3D woven SiC/SiC composite

Li *et al.* <sup>15</sup> investigated the cyclic tensile loading/unloading behavior of 2D woven CVI SiC/SiC composite at room temperature. The monotonic tensile stress/strain curve is given in Fig. 18. The composite tensile strength is about 268 MPa and the failure strain is 0.34 %. Under cyclic tensile loading/unloading, the stress/strain hysteresis loops of 2D woven SiC/SiC at different peak stresses of  $\sigma_{\max} = 152, 166, 181, 195, 210, 224, 239$  and  $253$  MPa are shown in Fig. 19a-h; with increasing peak stress, the damage parameter  $\eta$  (i.e. the proportion of matrix cracking mode 3) increases from  $\eta = 0.2$  at the peak stress of  $\sigma_{\max} = 152$  MPa to  $\eta = 0.65$  at the peak stress of  $\sigma_{\max} = 253$  MPa; the hysteresis dissipated energy increases from  $U_c = 2.3$  kPa at the peak stress of  $\sigma_{\max} = 152$  MPa to  $U_c = 45.4$  kPa at the peak stress of  $\sigma_{\max} = 253$  MPa; the hysteresis modulus decreases from  $E_a = 162$  GPa at the peak stress of  $\sigma_{\max} = 152$  MPa to  $E_a = 79.7$  GPa at the peak stress of  $\sigma_{\max} = 253$  MPa; the fiber/matrix interface debonding ratio ( $y/l_d$  and  $z/l_d$ ) corresponds to the fiber/matrix interface slip Case 1 at the peak stresses of  $\sigma_{\max} = 152, 166, 181, 195$

and  $210$  MPa, and the fiber/matrix interface slip Case 2 at the peak stresses of  $\sigma_{\max} = 224, 239$  and  $253$  MPa for matrix cracking mode 3, as shown in Fig. 20a-h; and for matrix cracking mode 5, the fiber/matrix interface debonding ratio ( $y/l_d$  and  $z/l_d$ ) corresponds to the fiber/matrix interface slip Case 1 at the peak stresses of  $\sigma_{\max} = 152, 166, 181, 195, 210, 224, 239$  and  $253$  MPa, as shown in Fig. 20a-h.

Simon *et al.* <sup>24</sup> investigated the cyclic tensile loading/unloading behavior of 2D woven CVI/PIP Nicalon<sup>TM</sup> NL 207 SiC/[Si-B-C] composite at room temperature. The monotonic tensile stress/strain curve is shown in Fig. 21. The composite tensile strength is about 250 MPa and the failure strain is 0.8 %. Under cyclic tensile loading/unloading, the stress/strain hysteresis loops of 2D woven SiC/[Si-B-C] at different peak stresses of  $\sigma_{\max} = 140, 157, 168, 180, 194$  and  $213$  MPa are shown in Fig. 22a-h; with increasing peak stress, the damage parameter  $\eta$  (i.e. the proportion of matrix cracking mode 3) increases from  $\eta = 0.3$  at the peak stress of  $\sigma_{\max} = 140$  MPa to  $\eta = 0.65$  at the peak stress of  $\sigma_{\max} = 213$  MPa; the hysteresis dissipated energy increases from  $U_c = 17.8$  kPa at the peak stress of  $\sigma_{\max} = 140$  MPa to  $U_c = 120.4$  kPa at the peak stress of  $\sigma_{\max} = 213$  MPa; the hysteresis modulus decreases from  $E_a = 84.4$  GPa at the peak stress of  $\sigma_{\max} = 140$  MPa to  $E_a = 37.1$  GPa at the peak stress of  $\sigma_{\max} = 213$  MPa; the fiber/matrix interface debonding ratio ( $y/l_d$  and  $z/l_d$ ) corresponds to the fiber/matrix interface slip Case 1 at the peak stress of  $\sigma_{\max} = 140$  MPa, the fiber/matrix interface slip Case 2 at the peak stresses of  $\sigma_{\max} = 157$  and  $168$  MPa, the fiber/matrix interface slip Case 3 at the peak stress of  $\sigma_{\max} = 180$  MPa, and the fiber/matrix interface slip Case 4 at the peak stresses of  $\sigma_{\max} = 194$  and  $213$  MPa for matrix cracking mode 3, as shown in Fig. 23a-f; and for matrix cracking mode 5, the fiber/matrix interface debonding ratio ( $y/l_d$  and  $z/l_d$ ) corresponds to the fiber/matrix interface slip Case 1 at the peak stresses of  $\sigma_{\max} = 140, 157, 168, 180, 194$  and  $213$  MPa, as shown in Fig. 23a-f.

Ogasawara *et al.* <sup>16</sup> investigated the cyclic tensile loading/unloading behavior of 3D woven Si-Ti-C-O fiber/Si-Ti-C-O matrix composite at room temperature. The monotonic tensile stress/strain curve is shown in Fig. 24. The composite tensile strength is about 423 MPa and the failure strain is 1.2 %. Under cyclic tensile loading/unloading, the stress/strain hysteresis loops of 3D woven SiC/SiC composite at different peak stresses of  $\sigma_{\max} = 205, 236, 265, 299, 328, 355$  and  $389$  MPa are shown in Fig. 25a-g; with increasing peak stress, the damage parameter  $\eta$  (i.e. the proportion of matrix cracking mode 3) increases from  $\eta = 0.35$  at the peak stress of  $\sigma_{\max} = 205$  MPa to  $\eta = 0.6$  at the peak stress of  $\sigma_{\max} = 389$  MPa; the hysteresis dissipated energy increases from  $U_c = 23.8$  kPa at the peak stress of  $\sigma_{\max} = 205$  MPa to  $U_c = 231.2$  kPa at the peak stress of  $\sigma_{\max} = 389$  MPa; the hysteresis modulus decreases from  $E_a = 63.9$  GPa at the peak stress of  $\sigma_{\max} = 205$  MPa to  $E_a = 39.5$  GPa at the peak stress of  $\sigma_{\max} = 389$  MPa; the fiber/matrix interface debonding ratio ( $y/l_d$  and  $z/l_d$ ) corresponds to the fiber/matrix interface slip Case 2 at the peak stresses of  $\sigma_{\max} = 205, 236, 265$  and  $299$  MPa, and the fiber/matrix interface slip Case 3 at the peak stresses



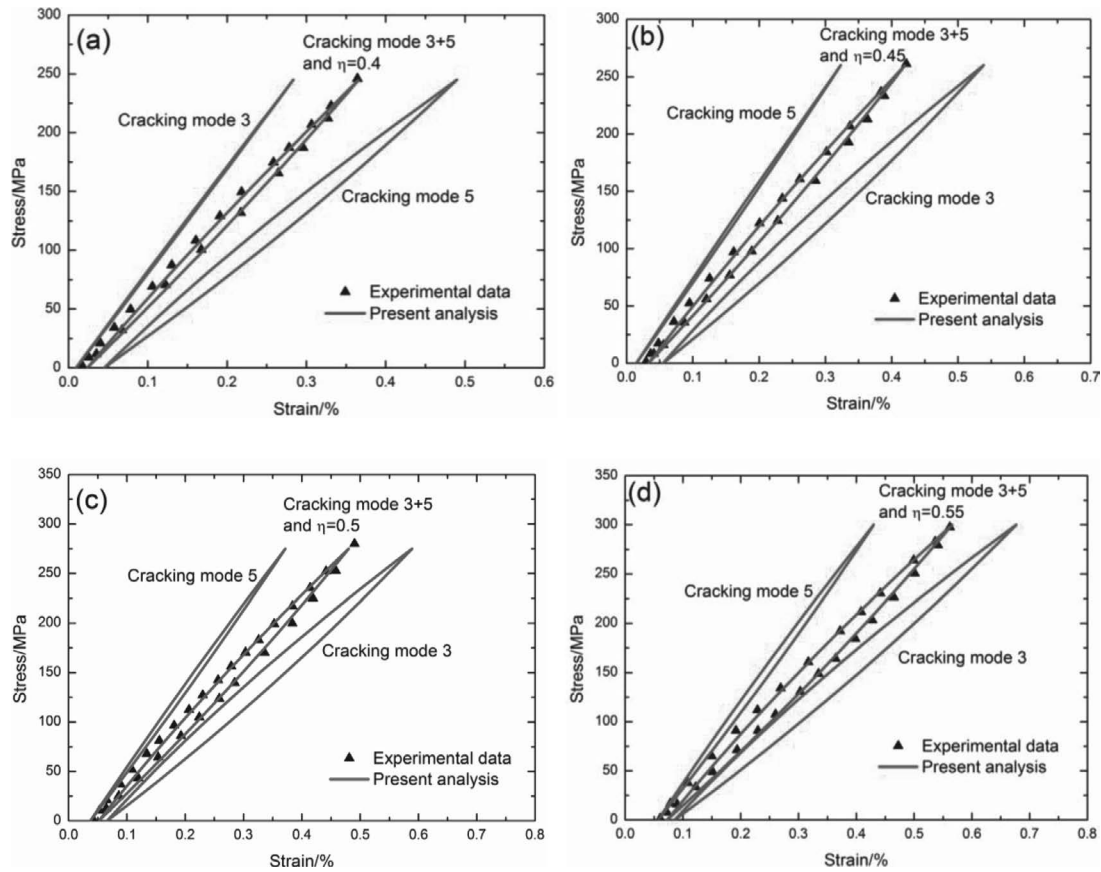


Fig. 13: The theoretical and experimental stress/strain hysteresis loops of 3D braided C/SiC composite<sup>11</sup> under cyclic loading corresponding to different peak stresses of (a)  $\sigma_{\max} = 245$  MPa; (b)  $\sigma_{\max} = 260$  MPa; (c)  $\sigma_{\max} = 275$  MPa; and (d)  $\sigma_{\max} = 300$  MPa.

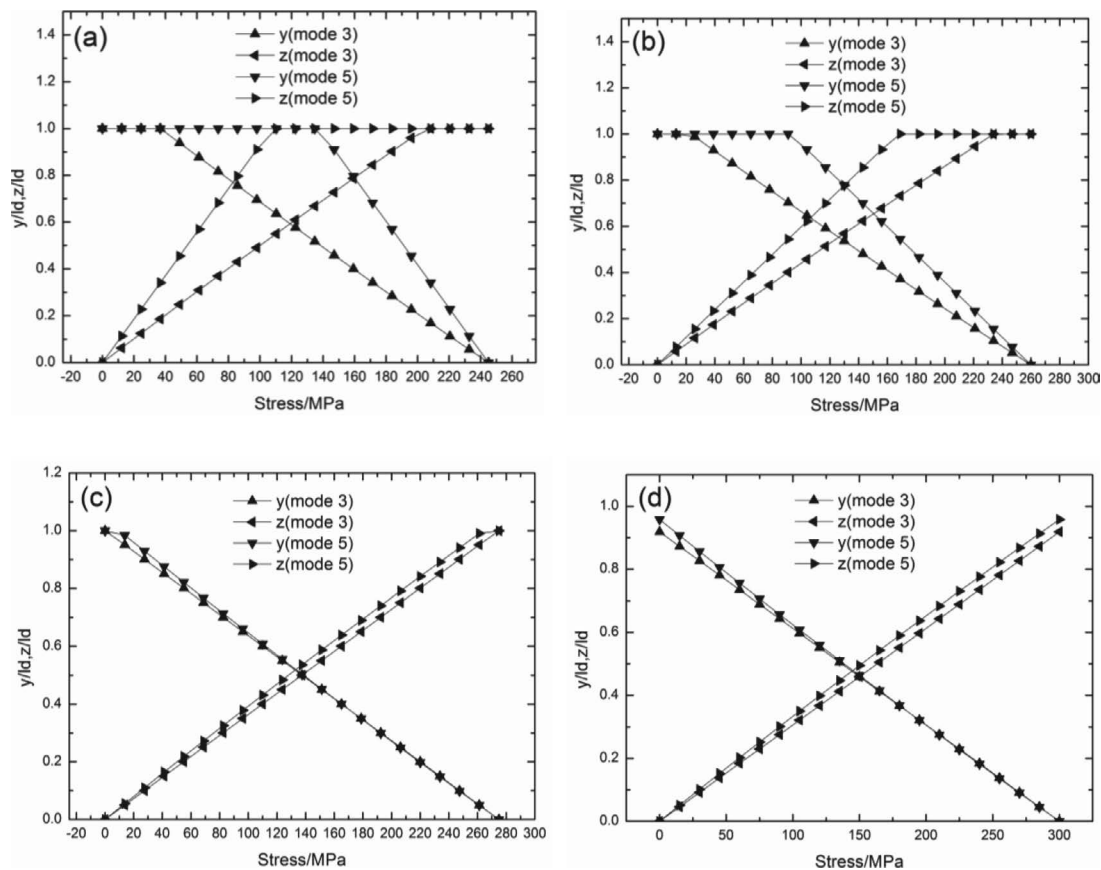


Fig. 14: The fiber/matrix interface sliding ratio ( $y/l_d$  and  $z/l_d$ ) of 3D braided C/SiC composite under cyclic loading corresponding to different peak stresses of (a)  $\sigma_{\max} = 245$  MPa; (b)  $\sigma_{\max} = 260$  MPa; (c)  $\sigma_{\max} = 275$  MPa; and (d)  $\sigma_{\max} = 300$  MPa.

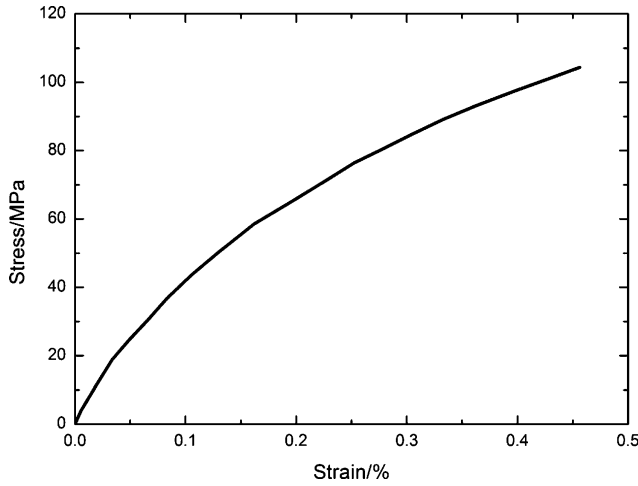


Fig. 15: The monotonic tensile stress/strain curve of 3D needled C/SiC composite <sup>13</sup>.

of  $\sigma_{\max} = 328, 355$  and  $389$  MPa for matrix cracking mode 3, as shown in Fig. 26a-g; and for matrix cracking mode 5, the fiber/matrix interface debonding ratio ( $y/l_d$  and  $z/l_d$ ) corresponds to the fiber/matrix interface slip Case 1 at the peak stress of  $\sigma_{\max} = 205$  MPa, and the fiber/

matrix interface slip Case 2 at the peak stresses of 236, 265, 299, 328, 355 and 389 MPa, as shown in Fig. 26a-g.

#### IV. Discussions

The damage accumulation comparisons between C/SiC and SiC/SiC composites with different fiber preforms, i.e. 2D and 2.5D woven, 3D braided and needled, are analyzed using damage parameters of matrix cracking mode ratio, hysteresis dissipated energy and hysteresis modulus.

##### (1) Damage accumulation comparisons between 2D and 2.5D woven, 3D braided and needled C/SiC composites

The damage parameter  $\eta$  (i.e., matrix cracking mode 3 proportion) versus normalized stress ( $\sigma_{\max}/\sigma_{UTS}$ ) curves of 2D and 2.5D woven, and 3D braided and needled C/SiC composites are shown in Fig. 27a. At low peak stress below  $60\% \sigma_{UTS}$ , the damage parameter  $\eta$  is the highest for 2.5D woven C/SiC composite along the warp direction; at high peak stress above  $60\% \sigma_{UTS}$ , the damage parameter  $\eta$  is the highest for 2D woven C/SiC composite; and the damage parameter  $\eta$  is the lowest for 3D needled C/SiC composite from low to high peak stress.

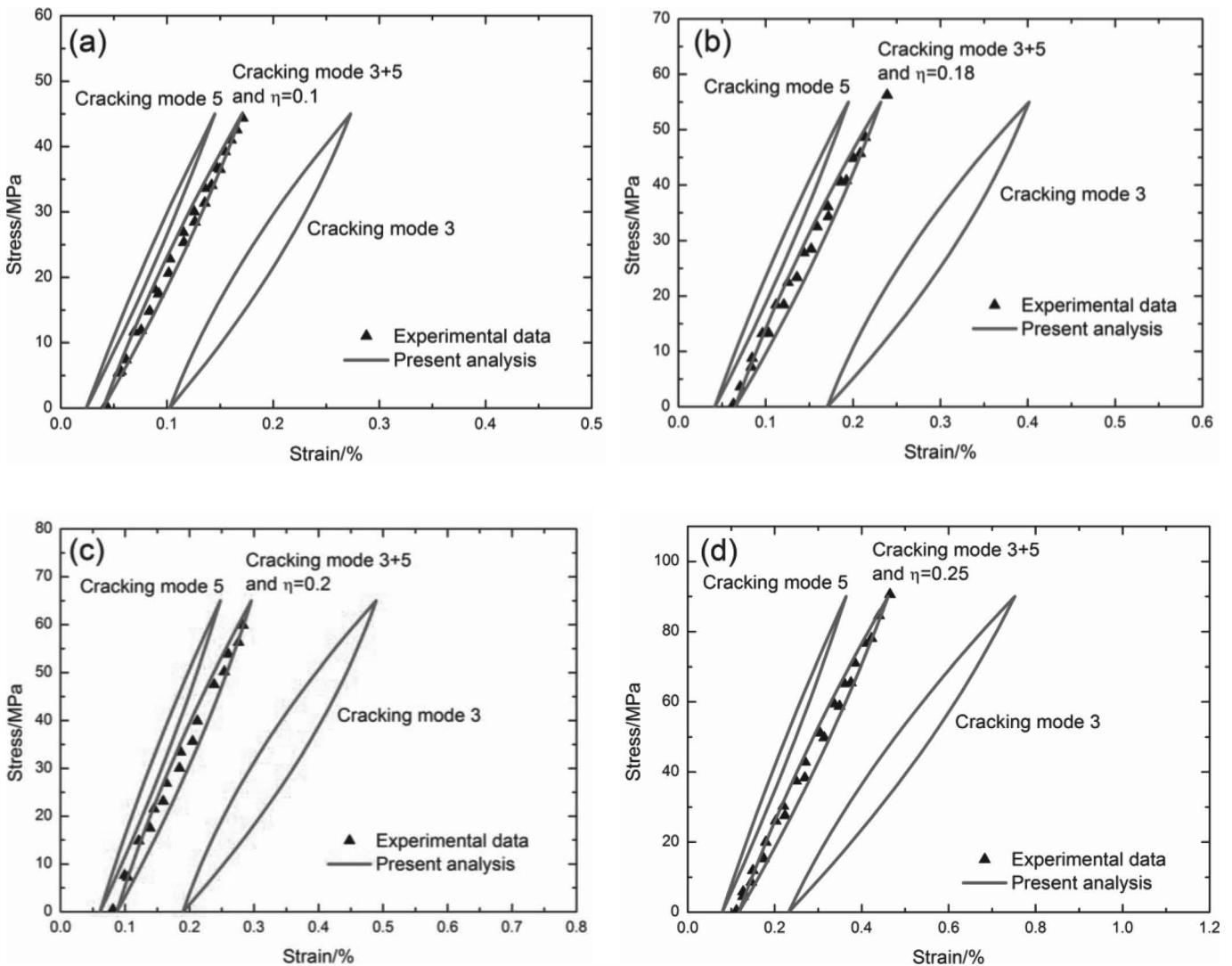


Fig. 16: The theoretical and experimental stress/strain hysteresis loops of 3D needled C/SiC composite <sup>13</sup> under cyclic loading corresponding to different peak stresses of (a)  $\sigma_{\max} = 45$  MPa; (b)  $\sigma_{\max} = 55$  MPa; (c)  $\sigma_{\max} = 65$  MPa; and (d)  $\sigma_{\max} = 90$  MPa.

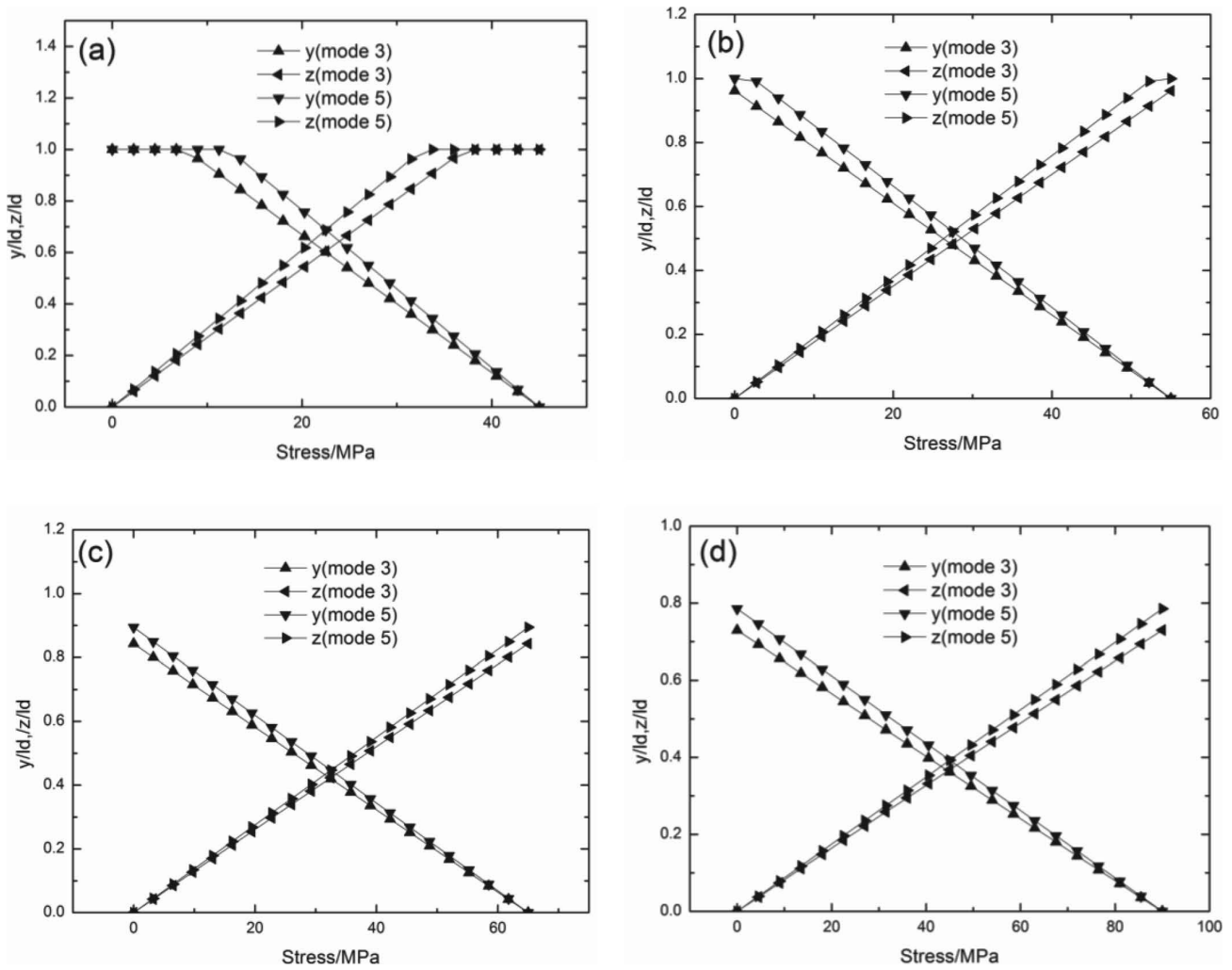


Fig. 17: The fiber/matrix interface sliding ratio ( $y/l_d$  and  $z/l_d$ ) of 3D needled C/SiC composite under cyclic loading corresponding to different peak stresses of (a)  $\sigma_{\max} = 45$  MPa; (b)  $\sigma_{\max} = 55$  MPa; (c)  $\sigma_{\max} = 65$  MPa; and (d)  $\sigma_{\max} = 90$  MPa.

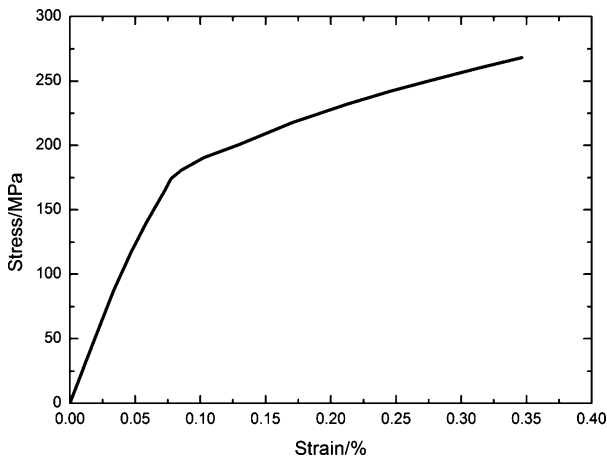


Fig. 18: The monotonic tensile stress/strain curve of 2D woven SiC/SiC composite<sup>15</sup>.

The hysteresis dissipated energy versus normalized stress ( $\sigma_{\max}/\sigma_{UTS}$ ) curves of 2D and 2.5D woven, 3D braided and needled C/SiC composites are given in Fig. 27b, in which the hysteresis dissipated energy increases with peak stress, due to the increase of damage parameter  $\eta$  and fiber/matrix interface sliding ratio. The hysteresis dissipated energy is the highest for 2.5D woven C/SiC composite along the warp direction, and the lowest for 3D needled C/SiC composite.

The hysteresis modulus versus normalized stress ( $\sigma_{\max}/\sigma_{UTS}$ ) curves of 2D and 2.5D woven, and 3D braided and needled C/SiC composites are given in Fig. 27c, in which the hysteresis modulus decreases with peak stress, due to multiple matrix cracking mode evolution and increase of fiber/matrix interface debonding ratio. The hysteresis modulus is the highest for 2.5D woven C/SiC composite along the warp direction, and the lowest for 3D needled C/SiC composite.

## (2) Damage accumulation comparisons between 2D and 3D woven SiC/SiC composites

The damage parameter  $\eta$  (i.e. matrix cracking mode 3 proportion) versus normalized stress ( $\sigma_{\max}/\sigma_{UTS}$ ) curves of 2D woven SiC/SiC, SiC/[Si-B-C] and 3D woven SiC/SiC composites are shown in Fig. 28a. At low peak stress below  $65\% \sigma_{UTS}$ , the damage parameter  $\eta$  is the highest for 3D woven SiC/SiC composite, at high peak stress above  $65\% \sigma_{UTS}$ , the damage parameter  $\eta$  is the highest for 2D woven SiC/[Si-B-C] composite; and the damage parameter  $\eta$  is the lowest for 2D woven SiC/SiC composite.

The hysteresis dissipated energy versus normalized stress ( $\sigma_{\max}/\sigma_{UTS}$ ) curves of 2D woven SiC/SiC, SiC/[Si-B-C] and 3D woven SiC/SiC composites are given in Fig. 28b. The hysteresis dissipated energy

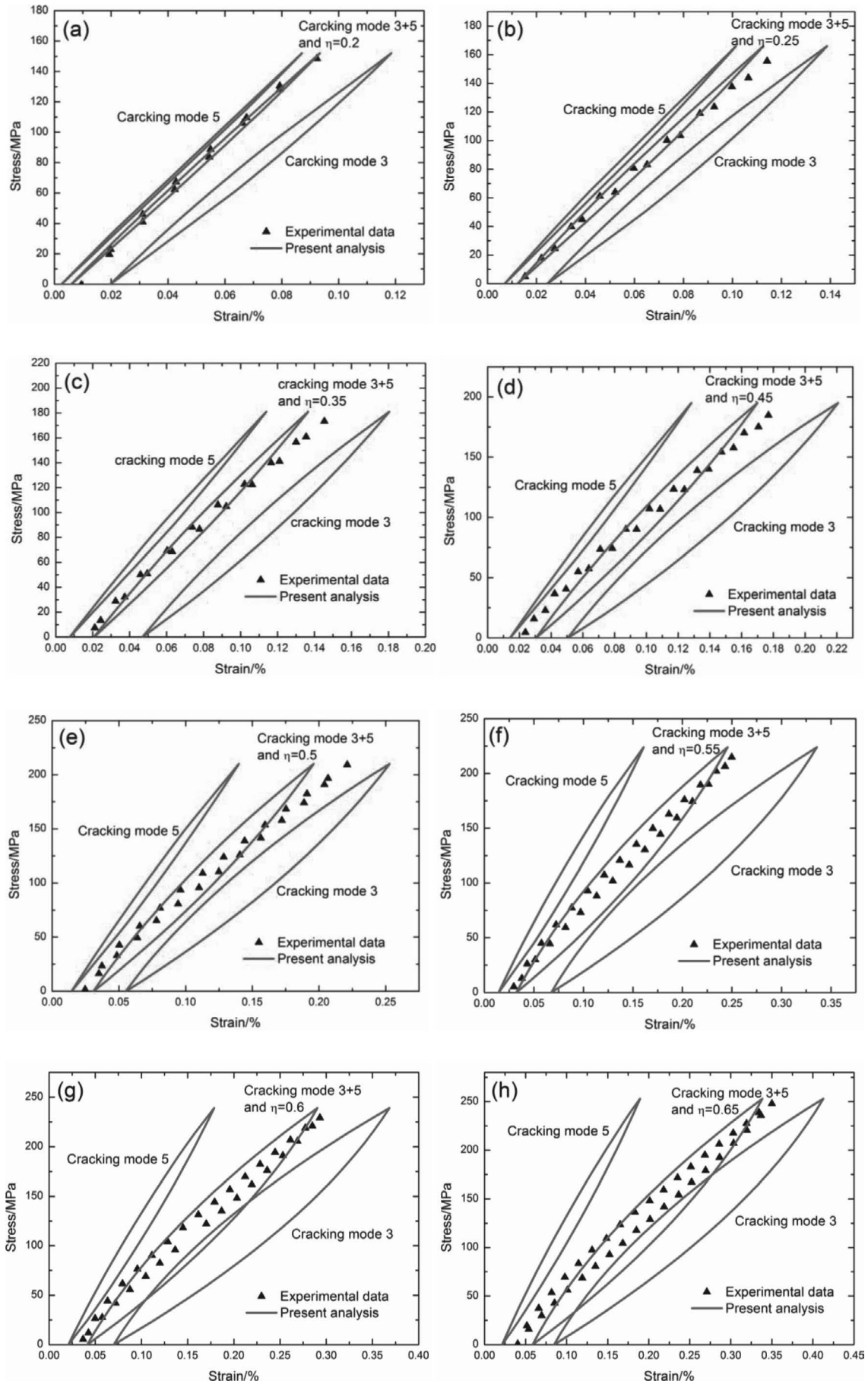


**Fig. 19:** The theoretical and experimental stress/strain hysteresis loops of 2D woven SiC/SiC composite<sup>15</sup> corresponding to different peak stresses of (a)  $\sigma_{\max} = 152$  MPa; (b)  $\sigma_{\max} = 166$  MPa; (c)  $\sigma_{\max} = 181$  MPa; (d)  $\sigma_{\max} = 195$  MPa; (e)  $\sigma_{\max} = 210$  MPa; (f)  $\sigma_{\max} = 224$  MPa; (g)  $\sigma_{\max} = 239$  MPa; and (h)  $\sigma_{\max} = 253$  MPa.

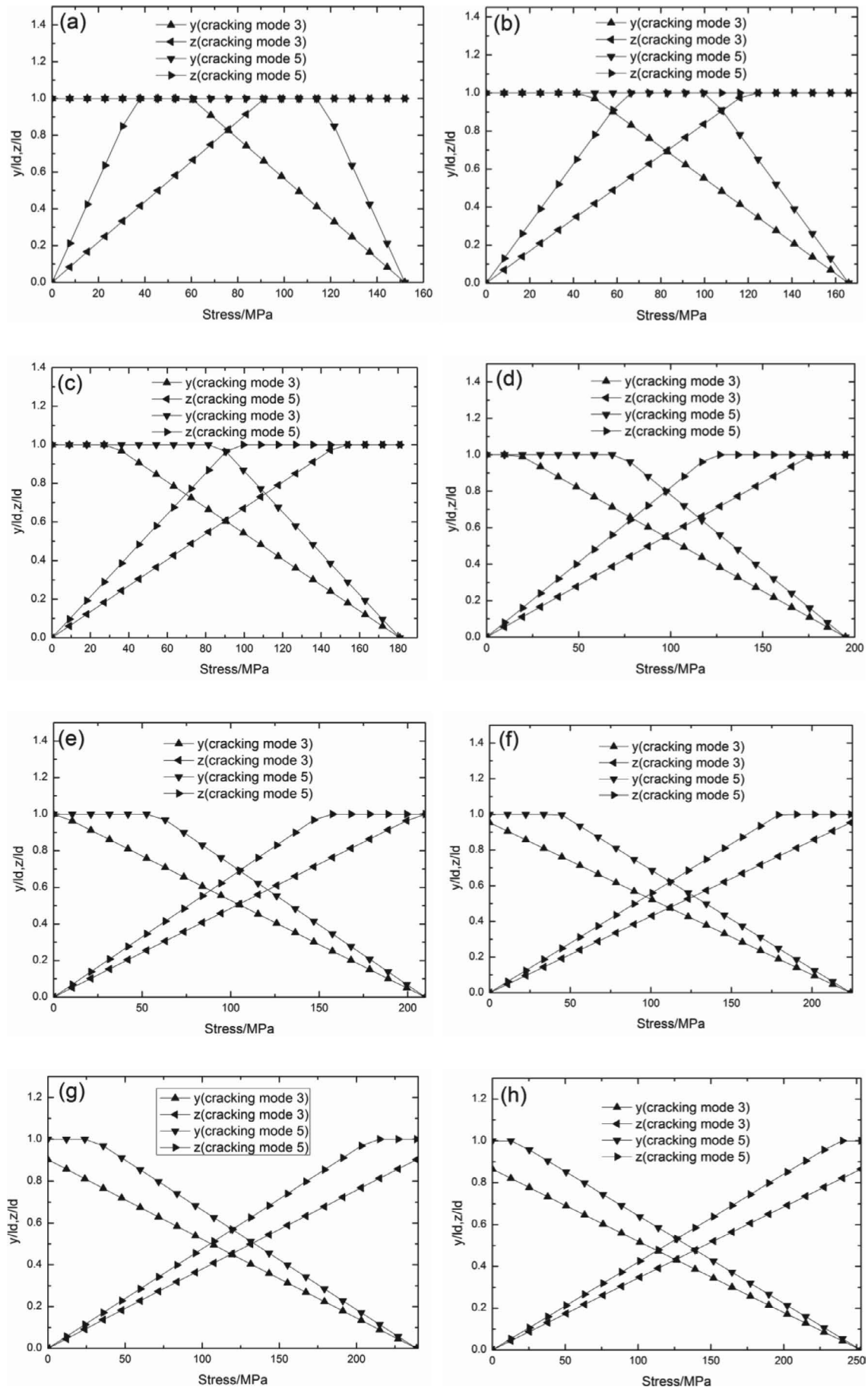


**Fig. 20:** The fiber/matrix interface sliding ratio ( $y/l_d$  and  $z/l_d$ ) of 2D woven SiC/SiC composite corresponding to different peak stresses of (a)  $\sigma_{\max} = 152$  MPa; (b)  $\sigma_{\max} = 166$  MPa; (c)  $\sigma_{\max} = 181$  MPa; (d)  $\sigma_{\max} = 195$  MPa; (e)  $\sigma_{\max} = 210$  MPa; (f)  $\sigma_{\max} = 224$  MPa; (g)  $\sigma_{\max} = 239$  MPa; and (h)  $\sigma_{\max} = 253$  MPa.



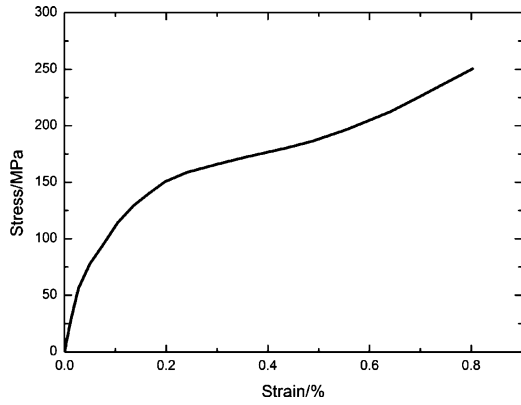


Fig. 21: The monotonic tensile stress/strain curve of 2D woven SiC/[Si-B-C] composite<sup>24</sup>.

is the highest for 3D woven SiC/SiC composite and the lowest for 2D woven SiC/SiC composite. The hysteresis dissipated energy of 2D woven SiC/[Si-B-C] composite

lies between that of 3D woven SiC/SiC and 2D woven SiC/SiC composite.

The hysteresis modulus versus normalized stress ( $\sigma_{\max}/\sigma_{\text{UTS}}$ ) curves of 2D woven SiC/SiC, SiC/[Si-B-C] and 3D woven SiC/SiC composites are given in Fig. 28c. The hysteresis modulus is the highest for 2D woven SiC/SiC composite and the lowest for 3D woven SiC/SiC composite. The hysteresis modulus of 2D woven SiC/[Si-B-C] composite lies between that of 2D woven SiC/SiC and 3D woven SiC/SiC composite.

### (3) Damage accumulation comparisons between 2D woven C/SiC and SiC/SiC composite

The damage parameter  $\eta$  (i.e. matrix cracking mode 3 proportion) versus normalized stress ( $\sigma_{\max}/\sigma_{\text{UTS}}$ ) curves of 2D woven C/SiC and SiC/SiC composites are shown in Fig. 29a. At low and high peak stress, the damage parameter  $\eta$  of C/SiC is higher than that of SiC/SiC composite, i.e.  $\eta = 0.3$  at  $\sigma_{\max} = 90$  MPa

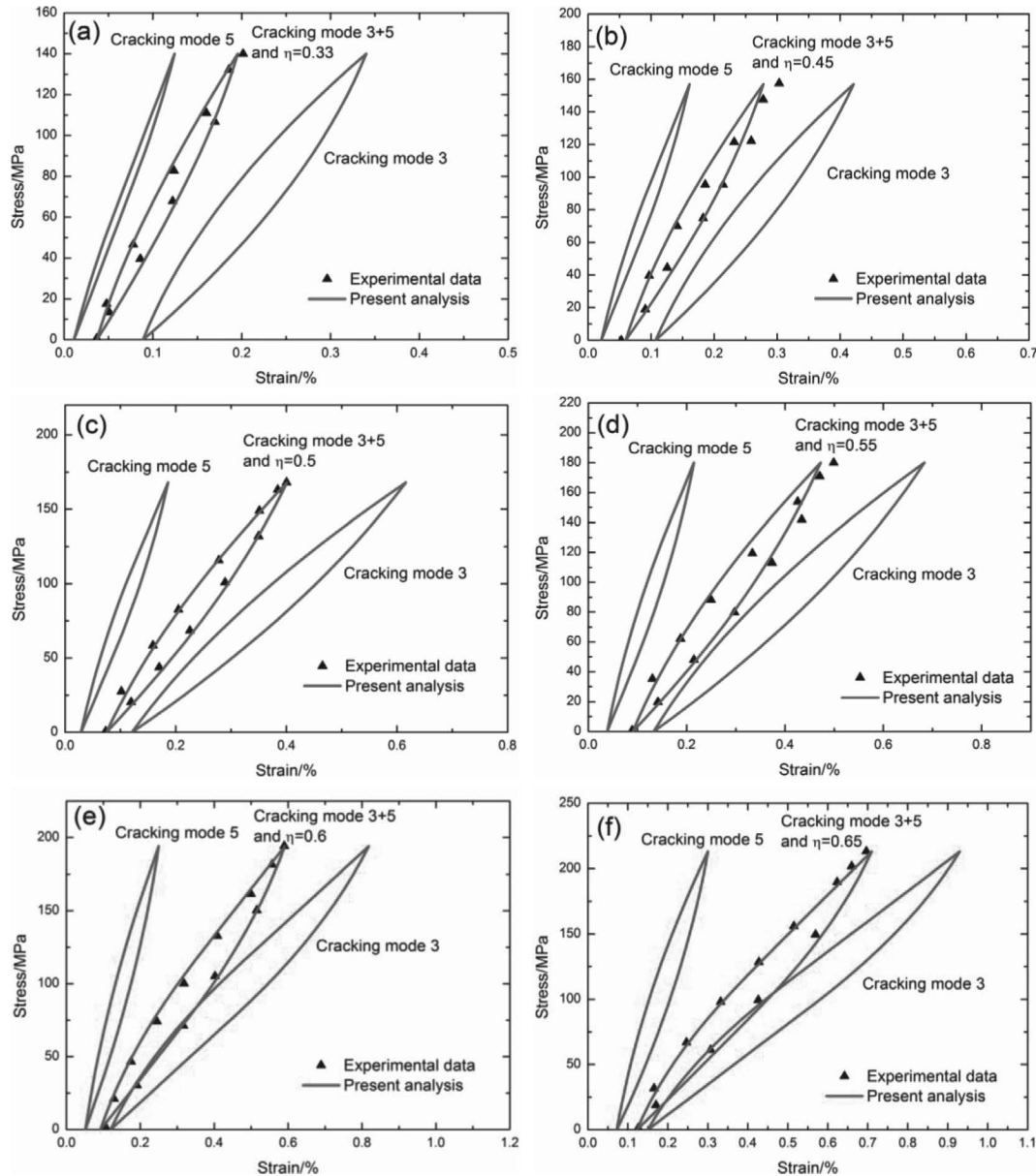
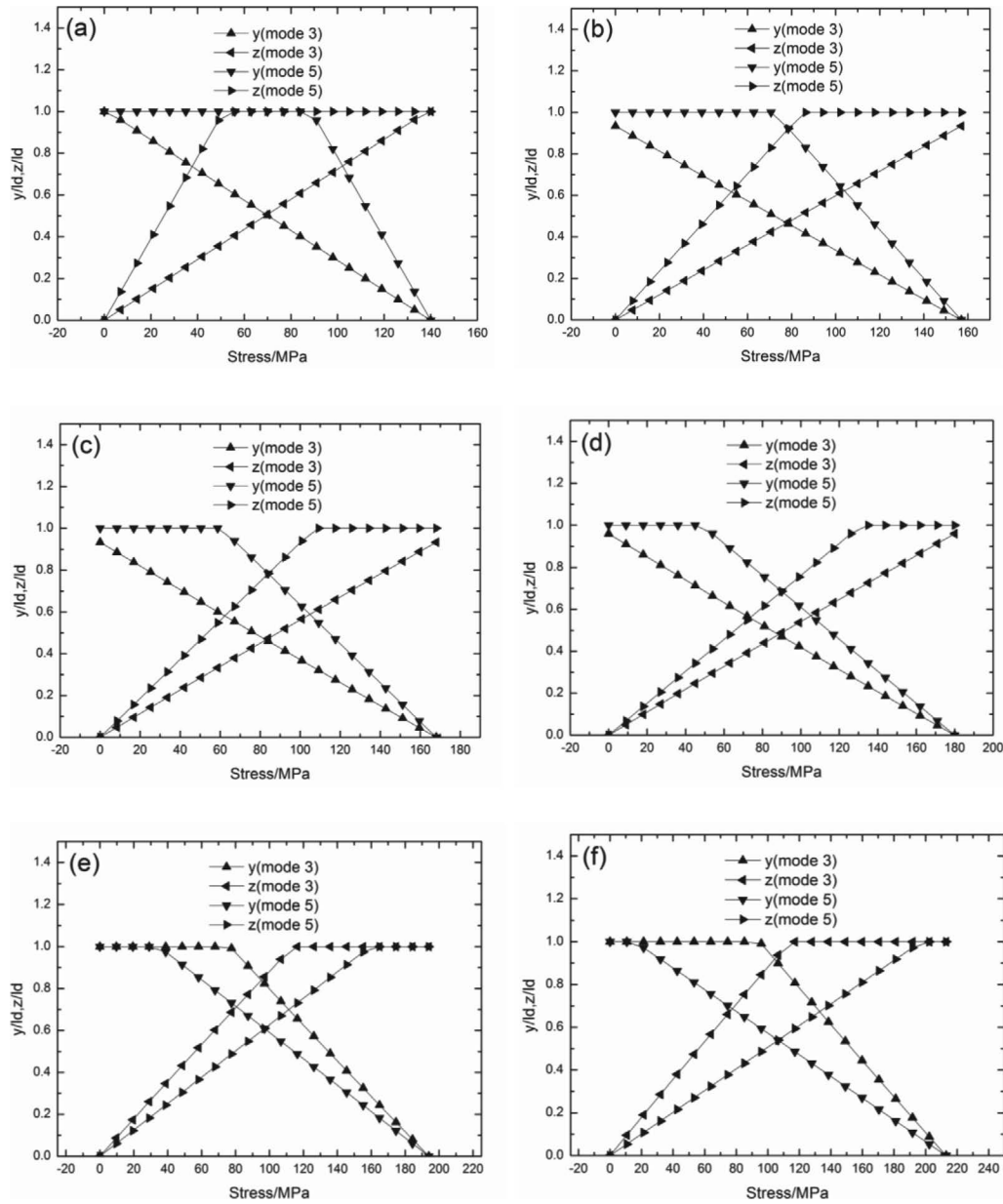


Fig. 22: The theoretical and experimental stress/strain hysteresis loops of 2D woven SiC/[Si-B-C] composite<sup>24</sup> corresponding to different peak stresses of (a)  $\sigma_{\max} = 140$  MPa; (b)  $\sigma_{\max} = 157$  MPa; (c)  $\sigma_{\max} = 168$  MPa; (d)  $\sigma_{\max} = 180$  MPa; (e)  $\sigma_{\max} = 194$  MPa; and (f)  $\sigma_{\max} = 213$  MPa.



**Fig. 23:** The fiber/matrix interface sliding ratio ( $y/l_d$  and  $z/l_d$ ) of 2D woven SiC/[Si-B-C] composite corresponding to different peak stresses of (a)  $\sigma_{\max} = 140$  MPa; (b)  $\sigma_{\max} = 157$  MPa; (c)  $\sigma_{\max} = 168$  MPa; (d)  $\sigma_{\max} = 180$  MPa; (e)  $\sigma_{\max} = 194$  MPa; and (f)  $\sigma_{\max} = 213$  MPa.

or 39 %  $\sigma_{\text{UTS}}$  of C/SiC, and  $\eta = 0.2$  at  $\sigma_{\max} = 152$  MPa or 56.7 %  $\sigma_{\text{UTS}}$  of SiC/SiC;  $\eta = 0.7$  at  $\sigma_{\max} = 210$  MPa or 91.3 %  $\sigma_{\text{UTS}}$  of C/SiC, and  $\eta = 0.65$  at  $\sigma_{\max} = 253$  MPa or 94.4 %  $\sigma_{\text{UTS}}$  of SiC/SiC. As the large mismatch of the axial thermal expansion coefficient between carbon fiber and silicon carbide matrix, i.e.  $0 \times 10^{-6}/\text{K}$  vs.  $a_m = 4.6 \times 10^{-6}/\text{K}$ , unavoidable microcracks existed within the SiC matrix in transverse and longitudinal yarns when the composite was cooled down from the high fabrication temperature to ambient temperature. These processing-induced microcracks propagated and, in conjunction with new microcracks during the loading process, formed mode 5 matrix cracks in the longitudinal yarns. With increasing applied stress, some matrix cracks in transverse yarns connected with matrix cracks in the longitudinal yarns forming mode 3 matrix cracks, which propagate through transverse and longitudinal yarns. However, for 2D woven SiC/SiC composite, the axial thermal residual compressive stress exist-

ed in SiC matrix, which decreases matrix cracking evolution rate and also the damage parameter  $\eta$ .

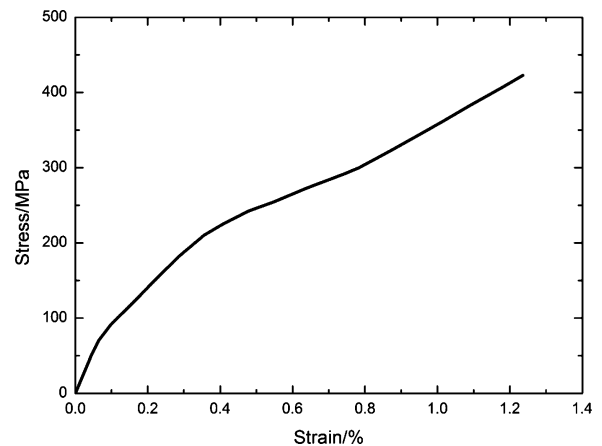


**Fig. 24:** The monotonic tensile stress/strain curve of 3D woven SiC/SiC composite <sup>16</sup>.

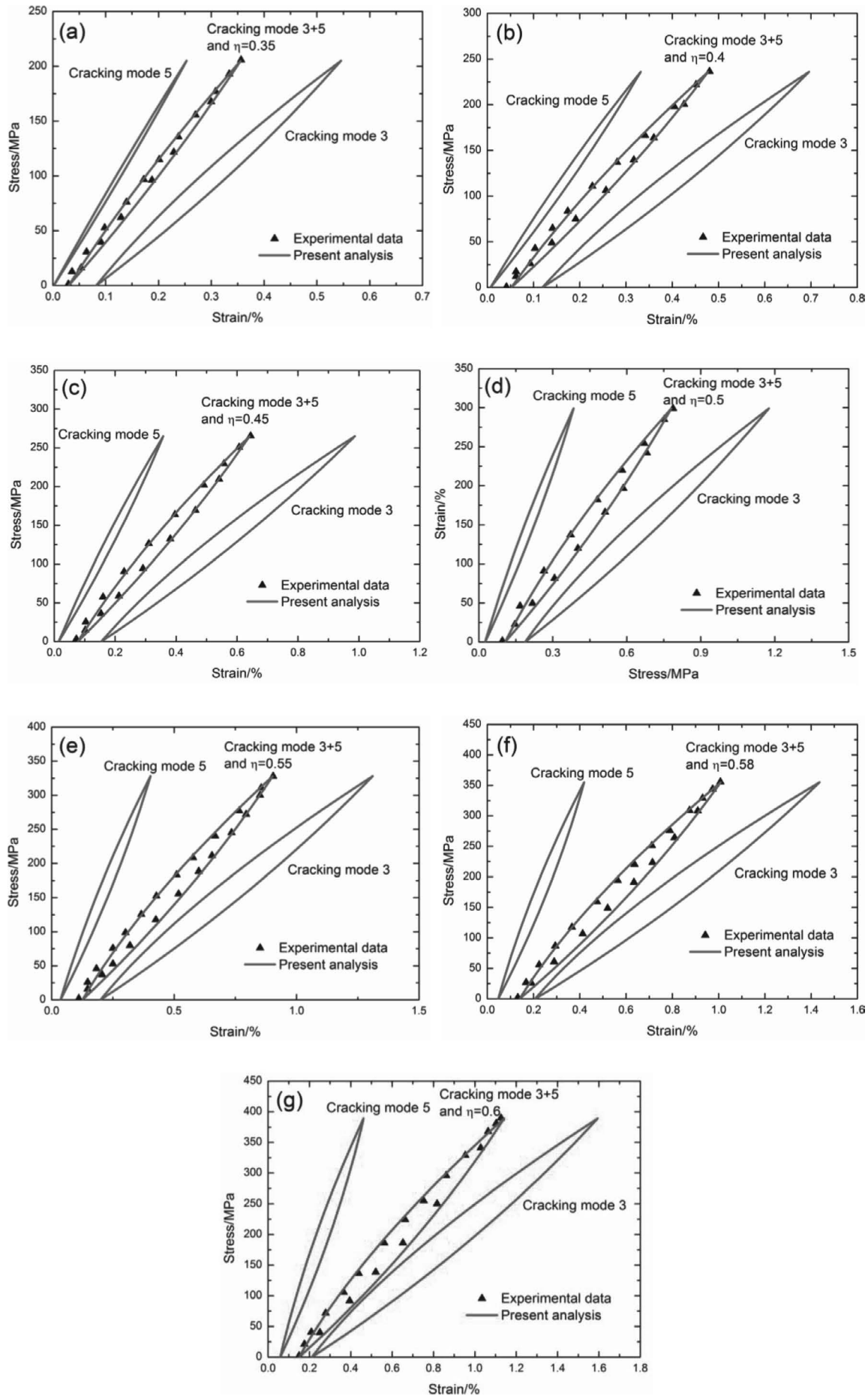


**Fig. 25:** The theoretical and experimental stress/strain hysteresis loops of 3D woven SiC/SiC composite<sup>16</sup> corresponding to different peak stresses of (a)  $\sigma_{\max} = 205$  MPa; (b)  $\sigma_{\max} = 236$  MPa; (c)  $\sigma_{\max} = 265$  MPa; (d)  $\sigma_{\max} = 299$  MPa; (e)  $\sigma_{\max} = 328$  MPa; (f)  $\sigma_{\max} = 355$  MPa; and (g)  $\sigma_{\max} = 389$  MPa.

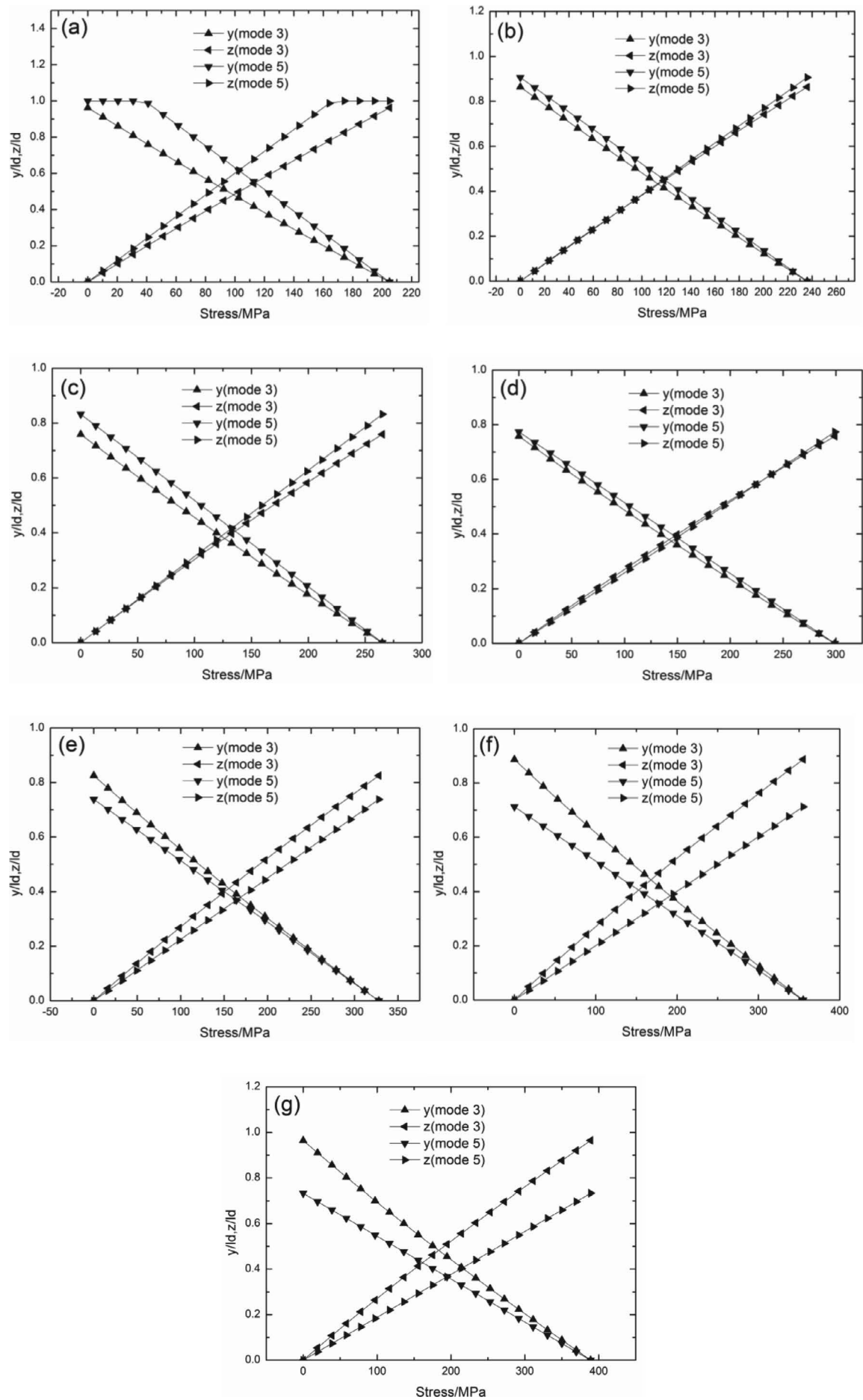


**Fig. 26:** The fiber/matrix interface sliding ratio ( $y/l_d$  and  $z/l_d$ ) of 3D woven SiC/SiC composite corresponding to different peak stresses of (a)  $\sigma_{\max} = 205$  MPa; (b)  $\sigma_{\max} = 236$  MPa; (c)  $\sigma_{\max} = 265$  MPa; (d)  $\sigma_{\max} = 299$  MPa; (e)  $\sigma_{\max} = 328$  MPa; (f)  $\sigma_{\max} = 355$  MPa; and (g)  $\sigma_{\max} = 389$  MPa.

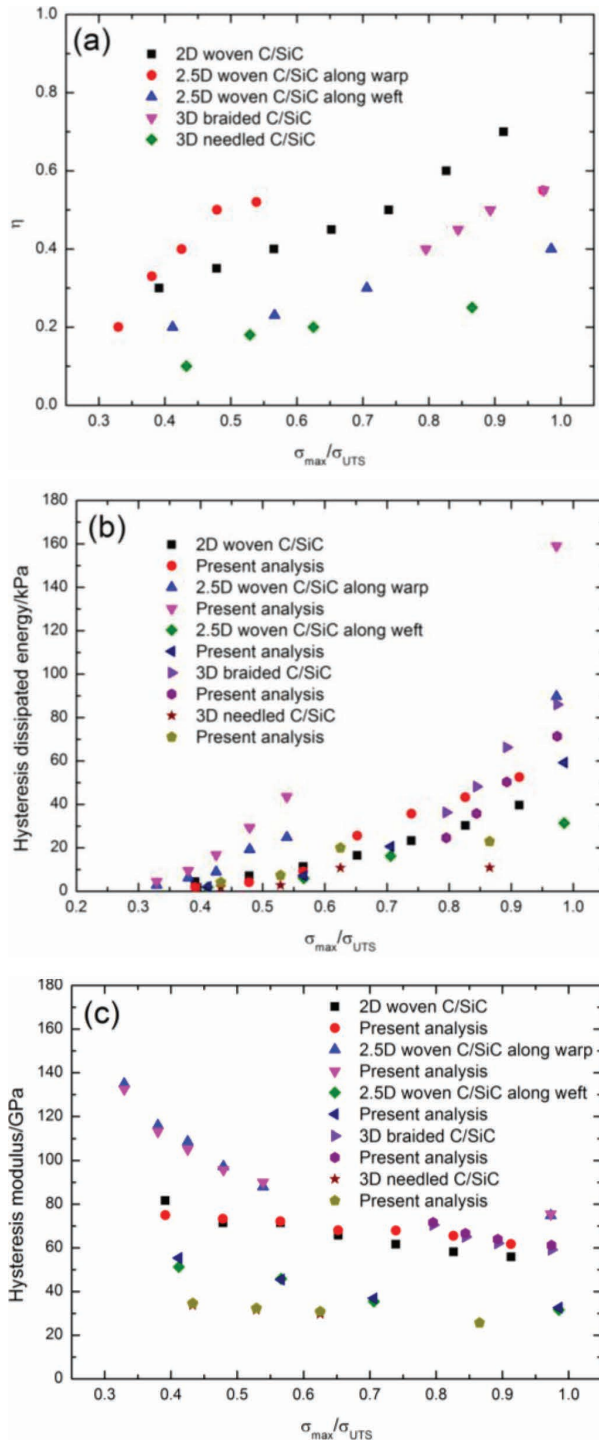


**Fig. 27:** (a) The damage parameter  $\eta$  versus normalized stress  $\sigma_{\max}/\sigma_{UTS}$  curves; (b) the experimental and theoretical hysteresis dissipated energy versus normalized stress  $\sigma_{\max}/\sigma_{UTS}$  curves; and (c) the experimental and theoretical hysteresis modulus versus normalized stress  $\sigma_{\max}/\sigma_{UTS}$  curves of 2D<sup>7</sup> and 2.5D<sup>10</sup> woven, 3D braided<sup>11</sup> and needled<sup>13</sup> C/SiC composites.

The experimental and theoretical hysteresis dissipated energy versus normalized stress ( $\sigma_{\max}/\sigma_{UTS}$ ) curves of 2D woven C/SiC and SiC/SiC are illustrated in Fig. 29b. With increasing peak stress, the hysteresis dissipated energy of C/SiC and SiC/SiC increases, i.e. from 4.4 kPa at  $\sigma_{\max} = 90$  MPa or 39.1 %  $\sigma_{UTS}$ , to 39.7 kPa at  $\sigma_{\max} = 210$  MPa or 91.3 %  $\sigma_{UTS}$  for C/SiC; and from 2.3 kPa at  $\sigma_{\max} = 152$  MPa or 56.7 %  $\sigma_{UTS}$ , to 45.4 kPa at  $\sigma_{\max} = 253$  MPa or 94.4 %  $\sigma_{UTS}$  for SiC/SiC. The experimental hysteresis

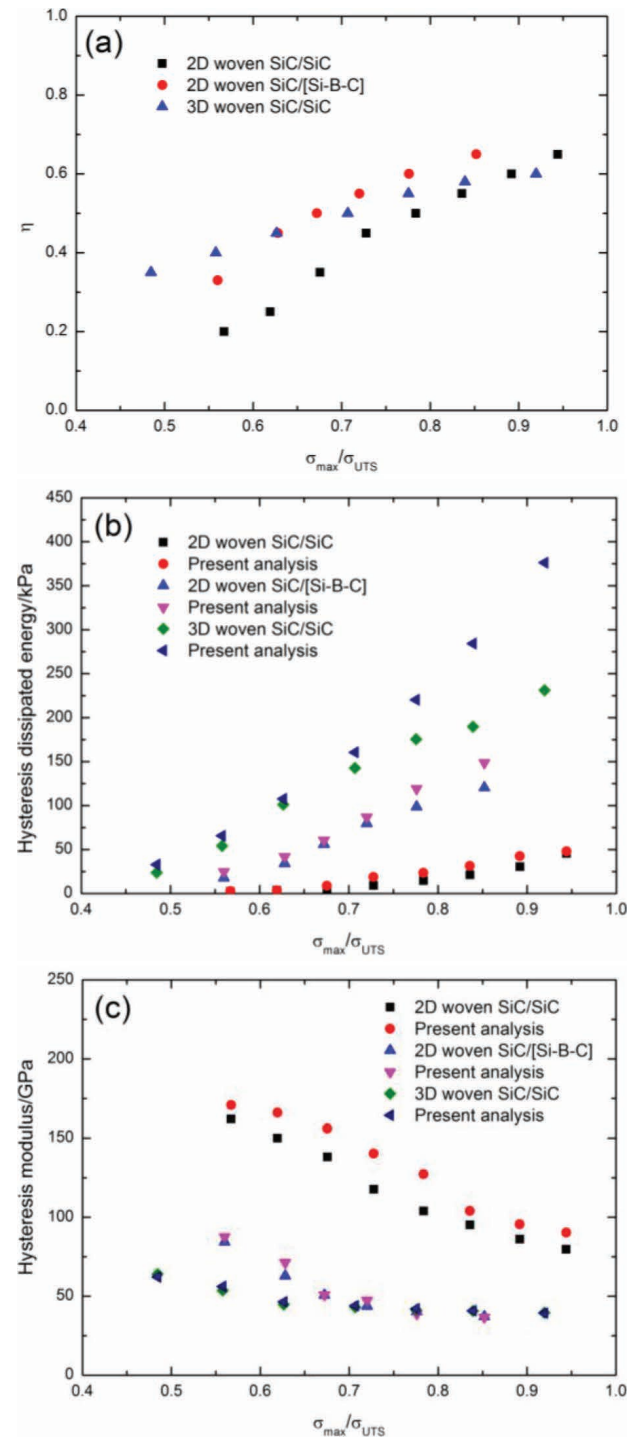


**Fig. 28:** (a) The damage parameter  $\eta$  versus normalized stress  $\sigma_{\max}/\sigma_{UTS}$  curves; (b) the experimental and theoretical hysteresis dissipated energy versus normalized stress  $\sigma_{\max}/\sigma_{UTS}$  curves; and (c) the experimental and theoretical hysteresis modulus versus normalized stress  $\sigma_{\max}/\sigma_{UTS}$  curves of 2D woven SiC/SiC<sup>15</sup> and SiC/[Si-B-C]<sup>24</sup>, and 3D woven SiC/SiC<sup>16</sup> composites.

dissipated energy of the C/SiC composite under low or high peak stresses is higher than that of the SiC/SiC, due to the higher damage parameter  $\eta$  and wider range of interface slip in the interface debonded region of C/SiC composite compared with those of SiC/SiC. For C/SiC, the hysteresis loops of matrix cracking mode 3 and mode 5 correspond to the fiber/matrix interface slip Case 2 and Case 1, respectively, under low peak stresses of 90, 110, and 130 MPa; when the peak stress is 150 MPa, the hys-



teresis loops of cracking mode 3 transfer from fiber/matrix interface slip Case 2 to Case 4; and when the peak stresses are 170, 190 and 210 MPa, the hysteresis loops of matrix cracking mode 3 and mode 5 correspond to the fiber/matrix interface slip Case 4 and Case 2. For SiC/SiC, the hysteresis loops of matrix cracking mode 3 and mode 5 correspond to the fiber/matrix interface slip Case 1 under low peak stresses of 152, 166, 181, 195 and 210 MPa; and when the peak stress increases to 224 MPa, the hysteresis loops of matrix cracking mode 3 transfer from fiber/matrix interface slip Case 1 to Case 2, and the hysteresis loops of matrix cracking mode 5 remain the fiber/matrix interface slip Case 1.

The experimental and theoretical hysteresis modulus versus normalized stress ( $\sigma_{\max}/\sigma_{\text{UTS}}$ ) curves of 2D woven C/SiC and SiC/SiC are illustrated in Fig. 29c, in which the hysteresis modulus decreases with increasing peak stress, i.e. for C/SiC, the hysteresis modulus decreases from 81.7 GPa at  $\sigma_{\max} = 90$  MPa or 39.1 %  $\sigma_{\text{UTS}}$ , to 55.9 GPa at  $\sigma_{\max} = 210$  MPa or 91.3 %  $\sigma_{\text{UTS}}$ ; and for SiC/SiC, the hysteresis modulus decreases from 162 GPa at  $\sigma_{\max} = 152$  MPa or 56.7 %  $\sigma_{\text{UTS}}$ , to 79.7 GPa at  $\sigma_{\max} = 253$  MPa or 94.4 %  $\sigma_{\text{UTS}}$ . The hysteresis modulus of the SiC/SiC composite is higher than that of the C/SiC composite at low and high peak stress, due to the matrix cracking caused by thermal residual stress, and the degradation

rate of the hysteresis modulus is higher for SiC/SiC than that of C/SiC, which indicates that matrix multicracking of SiC/SiC occurs with increasing peak stress.

#### (4) Damage accumulation comparisons between 3D braided and needled C/SiC and 3D woven SiC/SiC composite

The damage parameter  $\eta$  (i.e. matrix cracking mode 3 proportion) versus normalized stress ( $\sigma_{\max}/\sigma_{\text{UTS}}$ ) curves of 3D braided and needled C/SiC and 3D woven SiC/SiC composites are shown in Fig. 30a. The damage parameter  $\eta$  is the highest for 3D woven SiC/SiC composite and the lowest for 3D needled C/SiC composite.

The hysteresis dissipated energy versus normalized stress ( $\sigma_{\max}/\sigma_{\text{UTS}}$ ) curves of 3D braided and needled C/SiC and 3D woven SiC/SiC composites are shown in Fig. 30b. The hysteresis dissipated energy is the highest for 3D woven SiC/SiC composite and the lowest for 3D needled C/SiC composite.

The hysteresis modulus versus normalized stress ( $\sigma_{\max}/\sigma_{\text{UTS}}$ ) curves of 3D braided and needled C/SiC and 3D woven SiC/SiC composites are shown in Fig. 30c. The hysteresis modulus is the highest for 3D braided C/SiC composite and the lowest for 3D needled C/SiC composite.

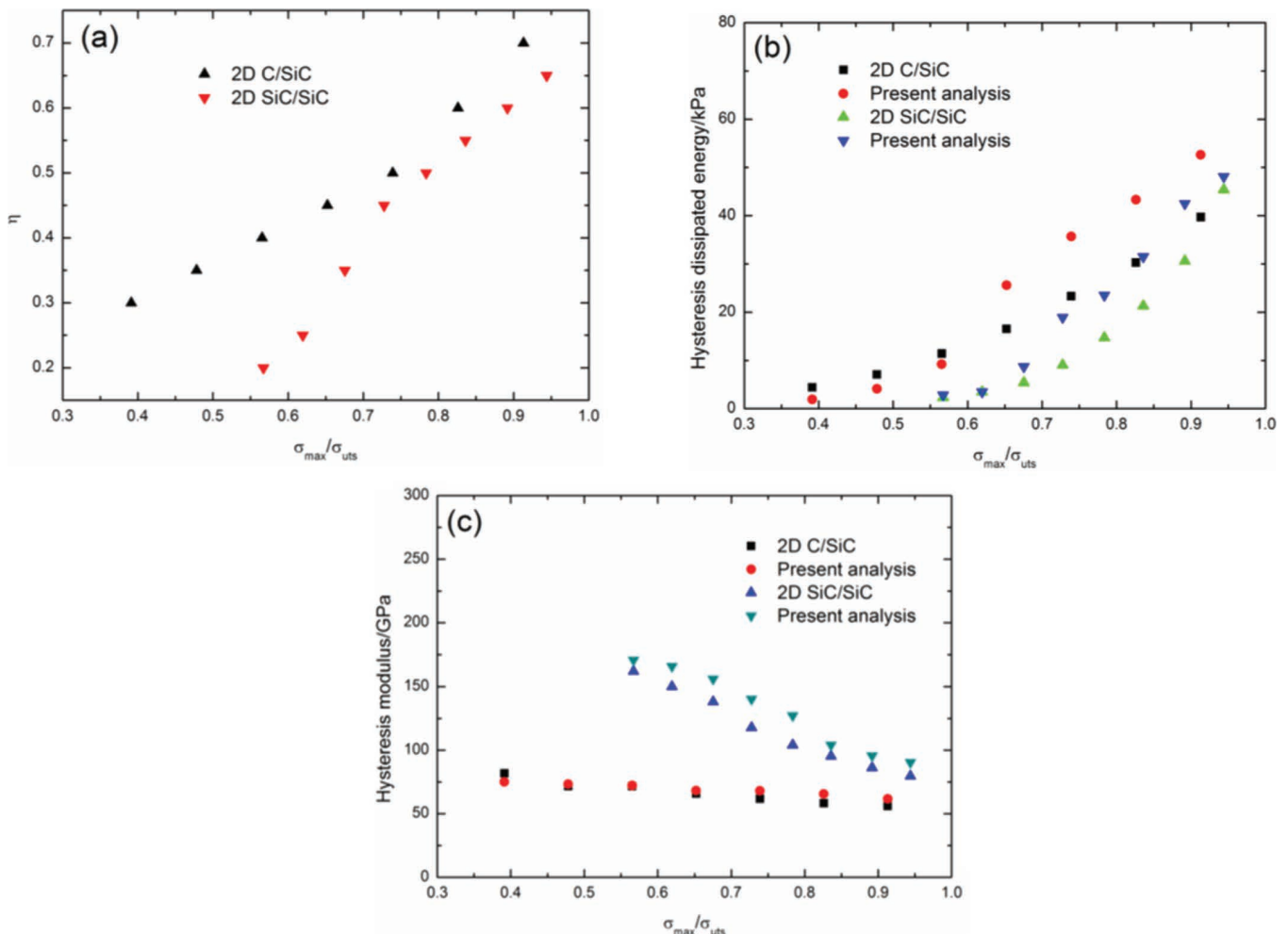


Fig. 29: (a) The damage parameter  $\eta$  versus normalized stress  $\sigma_{\max}/\sigma_{\text{UTS}}$  curves; (b) the experimental and theoretical hysteresis dissipated energy versus normalized stress  $\sigma_{\max}/\sigma_{\text{UTS}}$  curves; and (c) the experimental and theoretical hysteresis modulus versus normalized stress  $\sigma_{\max}/\sigma_{\text{UTS}}$  curves of 2D woven C/SiC<sup>7</sup> and SiC/SiC<sup>15</sup> composites.

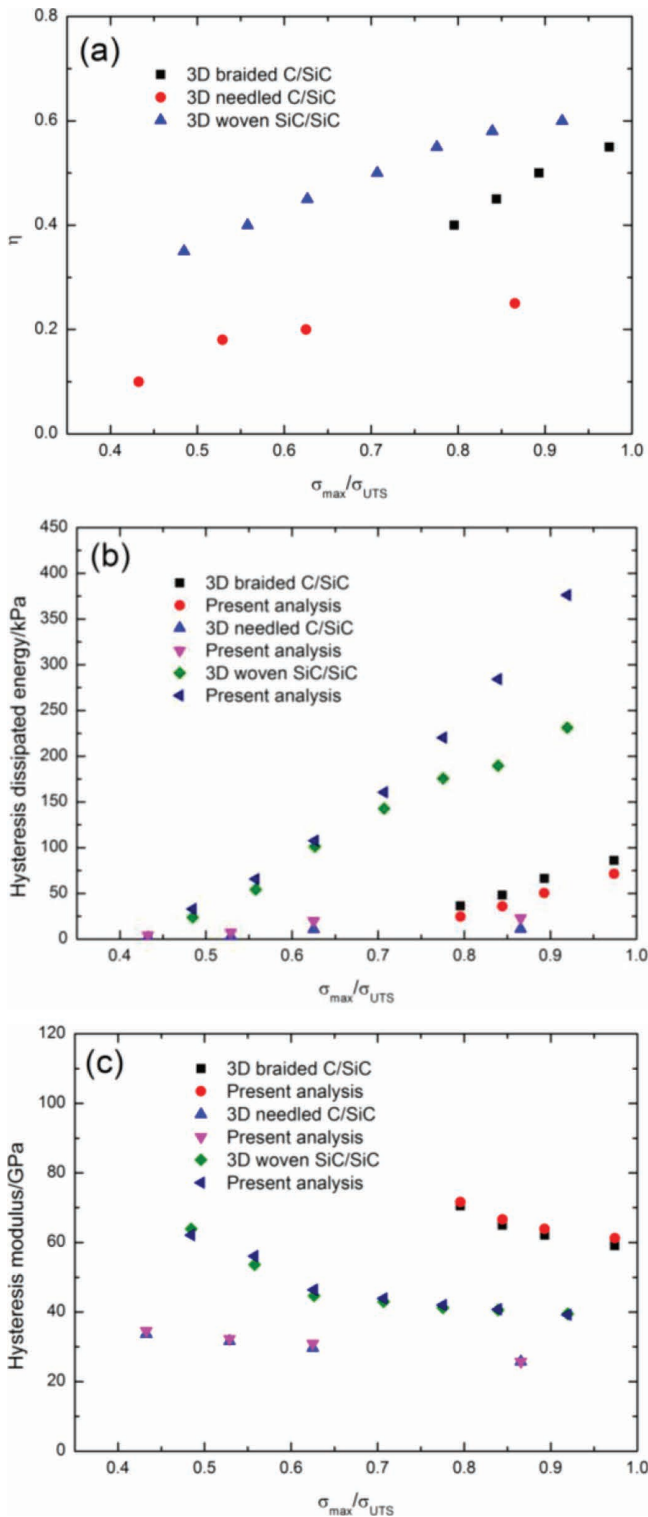


Fig. 30: (a) The damage parameter  $\eta$  versus normalized stress  $\sigma_{\max}/\sigma_{\text{UTS}}$  curves; (b) the experimental and theoretical hysteresis dissipated energy versus normalized stress  $\sigma_{\max}/\sigma_{\text{UTS}}$  curves; and (c) the experimental and theoretical hysteresis modulus versus normalized stress  $\sigma_{\max}/\sigma_{\text{UTS}}$  curves of 3D braided<sup>11</sup> and needled<sup>13</sup> C/SiC and 3D woven SiC/SiC<sup>16</sup> composites.

#### IV. Conclusions

The damage accumulation in 2D and 2.5D woven, 3D braided and needled C/SiC, 2D woven SiC/SiC and SiC/[Si-B-C], and 3D woven SiC/SiC composites under cyclic tensile loading/unloading has been investigated using damage parameters of matrix cracking mode ratio,

fiber/matrix interface sliding ratio and hysteresis-based damage parameters, i.e., hysteresis dissipated energy and hysteresis modulus. The damage comparisons between C/SiC and SiC/SiC with different fiber preforms have been analyzed.

- (1) Among 2D and 2.5D woven, 3D braided and needled C/SiC composites, at low peak stress below 60 %  $\sigma_{\text{UTS}}$ , the damage parameter  $\eta$  is the highest for 2.5D woven C/SiC composite along the warp direction; at high peak stress above 60 %  $\sigma_{\text{UTS}}$ , the damage parameter  $\eta$  is the highest for 2D woven C/SiC composite; and the damage parameter  $\eta$  is the lowest for 3D needled C/SiC composite from low to high peak stress.
- (2) Among 2D woven SiC/SiC and SiC/[Si-B-C], and 3D woven SiC/SiC composites, at low peak stress below 65 %  $\sigma_{\text{UTS}}$ , the damage parameter  $\eta$  is the highest for 3D woven SiC/SiC composite, at high peak stress above 65 %  $\sigma_{\text{UTS}}$ , the damage parameter  $\eta$  is the highest for 2D woven SiC/[Si-B-C] composite; and the damage parameter  $\eta$  is the lowest for 2D woven SiC/SiC composite.
- (3) Among 2D woven C/SiC and SiC/SiC composites, the experimental hysteresis dissipated energy of C/SiC composite under low or high peak stresses is higher than that of SiC/SiC, due to the higher damage parameter  $\eta$  and wider range of fiber/matrix interface slip in the fiber/matrix interface debonded region of C/SiC compared with those of SiC/SiC.
- (4) Among 3D braided and needled C/SiC and 3D woven SiC/SiC composites, the hysteresis dissipated energy is the highest for 3D woven SiC/SiC composite and the lowest for 3D needled C/SiC composite.

#### Acknowledgements

This work was supported by the Fundamental Research Funds for the Central Universities (Grant No. NS2016070). The author also wishes to thank two anonymous reviewers and editors for their helpful comments on an earlier version of the paper.

#### References

- 1 Naslain, R.: Design, preparation and properties of non-oxide CMCs for application in engines and nuclear reactors: an overview, *Compos. Sci. Tech.*, **64**, 155 - 170, (2004).
- 2 Shinavski, R.J.: Non-oxide/non-oxide ceramic matrix composites – composite design for tough behavior, *Comprehensive Composite Materials II*, **5**, 19–40, (2018).
- 3 Watanable, F., Nakamura, T., Mizokami, Y.: Design and testing for ceramic matrix composite turbine vane, Proceedings of ASME Turbo Expo 2017: Turbomachinery technical conference and exposition, June 26–30 2017, Charlotte NC USA.
- 4 Corman, G.S., Luthra, K.L.: Development history of GE's prepreg melt infiltrated ceramic matrix composite material and applications, *Comprehensive Composite Materials, II*, **5**, 325–338, (2018).
- 5 Pan, W.G., Jiao, G.Q., Guan, G.Y., Wang, B.: Tensile damage behavior of three dimensional braided C/SiC composites, *J. Chin. Ceram. Soc.*, **33**, 160–163, (2005).
- 6 Mei, H., Cheng, L.F., Zhang, L.T., Xu, Y.D., Meng, Z.X., Liu, C.D.: Damage evolution and microstructural characterization of a cross-woven C/SiC composite under tensile loading, *J. Chin. Ceram. Soc.*, **35**, 137–143, (2007).

- 7 Wang, Y.Q., Zhang, L.T., Cheng, L.F., Mei, H., Ma, J.Q.: Characterization of tensile behavior of a two-dimensional woven carbon/silicon carbide composite fabricated by chemical vapor infiltration, *Mater. Sci. Eng. A*, **497**, 295–300, (2008).
- 8 Wang, Y.Q., Zhang, L.T., Cheng, L.F., Ma, J.Q., Zhang, W.H.: Tensile performance and damage evolution of a 2.5D C/SiC composite characterized by acoustic emission. *Appl. Compos. Mater.*, **15**, 183–188, (2008).
- 9 Liu, C.D., Cheng, L.F., Luan, X.G., Li, B., Zhou, J.: Damage evolution and real-time non-destructive evaluation of 2D carbon-fiber/SiC-matrix composites under fatigue loading. *Mater. Lett.*, **62**, 3922–3924, (2008).
- 10 Chang, Y.J., Jiao, G.Q., Tao, Y.Q., Wang, B.: Damage behavior of 2.5-C/SiC composite under tensile loading, *J. Inorg. Mater.*, **23**, 509–514, (2008).
- 11 Mei, H., Cheng, L.F.: Comparison of the mechanical hysteresis of carbon/ceramic matrix composites with different fiber pre-forms, *Carbon*, **47**, 1034–1042, (2009).
- 12 Nie, J., Xu, Y., Wan, Y., Zhang, L.T., Cheng, L.F., Ma, J.Q.: Tensile behavior of three-dimensional needled carbon fiber reinforced SiC composite under load-unload, *J. Chin. Ceram. Soc.*, **37**, 76–82, (2009).
- 13 Xie, J., Fang, G., Chen, Z., Liang, J.: Modeling of nonlinear mechanical behavior for 3D needled C/C-SiC composites under tensile load, *Appl. Compos. Mater.*, **23**, 783–797, (2016).
- 14 Cheng, Q., Tong, X., Chen, L., Yao, L., Li, B.: Mechanical property and damage behavior of silicon carbide composites toughened by carbon fibers plain-woven, *J. Chin. Ceram. Soc.*, **38**, 931–937, (2010).
- 15 Li, P., Wang, B., Zhen, W., Jiao, G.: Tensile loading/unloading stress-strain behavior of 2D-SiC/SiC composites, *Acta Mater. Compos. Sinica*, **31**, 676–682, (2014).
- 16 Ogasawara, T., Ishikawa, T., Ito, H., Watanabe, N.: Multiple cracking and tensile behavior for an orthogonal 3-D woven silti-C-O fiber/Si-Ti-C-O matrix composite, *J. Am. Ceram. Soc.*, **84**, 1565–1574, (2001).
- 17 Li, Y., Xiao, P., Li, Z., Zhou, W., Liensdorf, T., Freudenberger, W., Langhof, N., Krenkel, W.: Tensile fatigue behavior of plain-weave reinforced C/C-SiC composites, *Ceram. Int.*, **42**, 6850–6857 (2016).
- 18 Li, Y., Xiao, P., Li, Z., Zhou, W., Liensdorf, T., Freudenberger, W., Reicher, F., Langhof, N., Krenkerl, W.: Strength evolution of cyclic load LSI-based C/C-SiC composites. *Ceram. Int.*, **42**, 14505–14510, (2016).
- 19 Luo, Z., Cao, H., Ren, H., Zhou, X.: Tension-tension fatigue behavior of a PIP SiC/SiC composite at elevated temperature in air, *Ceram. Int.*, **42**, 3250–3260, (2016).
- 20 Whitlow, T., Jones, E., Przybyla, C.: *In-situ* damage monitoring of a SiC/SiC ceramic matrix composite using acoustic emission and digital image correlation, *Compos. Struct.*, **158**, 245–251, (2016).
- 21 Momon, S., Moevus, M., Godin, N., R'Mili, M., Reynaud, P., Fantozzi, G., Fayolle, G.: Acoustic emission and lifetime prediction during static fatigue tests on ceramic-matrix composite at high temperature under air, *Compos. Part A*, **41**, 913–918, (2010).
- 22 Smith, C.E., Morscher, G.N., Xia, Z.H.: Monitoring damage accumulation in ceramic matrix composites using electrical resistivity, *Scripta Mater.*, **59**, 463–466, (2008).
- 23 Mansour, R., Maillet, E., Morscher, G.N.: Monitoring interlaminar crack growth in ceramic matrix composites using electrical resistance, *Scripta Mater*, **98**, 9–12, (2015).
- 24 Simon, C., Rebillat, F., Herb, V., Camus, G.: Monitoring damage evolution of SiC<sub>f</sub>/[Si-B-C]<sub>m</sub> composites using electrical resistivity: crack density-based electromechanical modeling, *Acta Mater.*, **124**, 579–587, (2017).
- 25 Simon, C., Rebillat, F., Camus, G.: Electrical resistivity monitoring of a SiC/[Si-B-C] composite under oxidizing environments, *Acta Mater.*, **132**, 586–597, (2017).
- 26 Chateau, C., Gelebart, L., Bornert, M., Crepin, J., Boller, E., Sauder, C., Ludwig, W.: In situ X-ray microtomography characterization of damage in SiC<sub>f</sub>/SiC minicomposites, *Compos. Sci. Technol.*, **71**, 916–924, (2011).
- 27 Vagaggini, E., Domergue, J.M., Evans, A.G.: Relationships between hysteresis measurements and the constituent properties of ceramic matrix composites: I, Theory, *J. Am. Ceram. Soc.*, **78**, 2709–2720, (1995).
- 28 Domergue, J.M., Vagaggini, E., Evans, A.G.: Relationships between hysteresis measurements and the constituent properties of ceramic matrix composites: II, Experimental studies on unidirectional materials, *J. Am. Ceram. Soc.*, **78**, 2721–2731, (1995).
- 29 Solti, J.P., Mall, S., Robertson, D.D.: Modeling damage in unidirectional ceramic-matrix composites, *Compos. Sci. Technol.*, **54**, 55–66, (1995).
- 30 Reynaud, P.: Cyclic fatigue of ceramic-matrix composites at ambient and elevated temperatures, *Compos. Sci. Technol.*, **56**, 809–814, (1996).
- 31 Cho, C.: Relationship between frictional heating and micro-failure state in a continuous fiber-reinforced ceramic matrix composite under cyclic loading, *J. Mater. Sci. Lett.*, **18**, 463–466, (1999).
- 32 Li, L.B.: Modeling the effect of interface wear on fatigue hysteresis behavior of carbon fiber-reinforced ceramic-matrix composites, *Appl. Compos. Mater.*, **22**, 887–920, (2015).
- 33 Li, L.B.: Modeling the effect of oxidation on hysteresis loops of carbon fiber-reinforced ceramic-matrix composites under static fatigue at elevated temperature, *J. Eur. Ceram. Soc.*, **36**, 465–480, (2016).
- 34 Li, L.B.: Modeling cyclic fatigue hysteresis loops of 2D woven ceramic-matrix composites at elevated temperature in steam, *Materials*, **9**, 421, (2016).
- 35 Campbell, C.X., Jenkins, M.G.: Use of unload/reload methodologies to investigate the thermal degradation of an alumina fiber-reinforced ceramic matrix composites. Symposium on Environmental, Mechanical, and Thermal Properties and Performance of Continuous Fiber Ceramic Composite (CFCC) Materials and Components, Seattle, Washington, May 18, 1999.
- 36 Mei, H.: Measurement and calculation of thermal residual stress in fiber reinforced ceramic matrix composites. *Compos. Sci. Tech.*, **68**, 3285–3292, (2008).
- 37 Fantozzi, G., Reynaud, P.: Mechanical hysteresis in ceramic matrix composites. *Mater. Sci. Eng. A*, **521–522**, 18–23, (2009).
- 38 Kuo, W.S., Chou, T.W.: Multiple cracking of unidirectional and cross-ply ceramic matrix composites, *J. Am. Ceram. Soc.*, **78**, 745–755, (1995).
- 39 Lamon, J.: A micromechanics-based approach to the mechanical behavior of brittle-matrix composites, *Compos. Sci. Technol.*, **61**, 2259–2272, (2001).
- 40 Dalmaz, A., Reynaud, P., Rouby, D., Fantozzi, G., Abbe, F.: Mechanical behavior and damage development during cyclic fatigue at high-temperature of a 2.5D carbon/SiC composite, *Compos. Sci. Technol.*, **58**, 693–699, (1998).
- 41 Nasiri, N.A., Patra, N., Ni, N., Jayaseelan, D.D., Lee, W.E.: Oxidation behavior of SiC/SiC ceramic matrix composites in air, *J. Eur. Ceram. Soc.*, **36**, 3293–3302, (2016).
- 42 Halbig, M.C., McGuffin-Cawley, J.D., Eckel, A.J., Brewer, D.N.: Oxidation kinetics and stress effects for the oxidation of continuous carbon fibers within a microcracked C/SiC ceramic matrix composite, *J. Am. Ceram. Soc.*, **91**, 519–526, (2008).

- <sup>43</sup> Rouby, D., Reynaud, P.: Fatigue behavior related to interface modification during load cycling in ceramic-matrix fiber composites, *Compos. Sci. Technol.*, **48**, 109–118, (1993).
- <sup>44</sup> Evans, A.G., Zok, F.W., McMeeking, R.M.: Fatigue of ceramic matrix composites. *Acta Metall. Mater.*, **43**, 859–875, (1995).
- <sup>45</sup> Zhu, S.J., Mizuno, M., Kagawa, Y., Mutoh, Y.: Monotonic tension, fatigue and creep behavior of SiC-fiber-reinforced SiC-matrix composites: a review, *Compos. Sci. Technol.*, **59**, 833–851, (1999).
- <sup>46</sup> McNulty, J.C., Zok, F.W.: Low-cycle fatigue of Nicalon<sup>TM</sup>-fiber-reinforced ceramic composites, *Compos. Sci. Technol.*, **59**, 1597–1607, (1999).
- <sup>47</sup> Dassios, K.G., Aggelis, D.G., Kordatos, E.Z., Matikas, T.E.: Cyclic loading of a SiC-fiber reinforced ceramic matrix composite reveals damage mechanisms and thermal residual stress state, *Compos. Part A*, **44**, 105–113, (2013).

